FEF inactivation with improved optogenetic methods

Leah Acker[a,b,c,1], Erica N. Pino[a,d,e], Edward S. Boyden[a,f,g,h], and Robert Desimone[a,f,1]

[a]McGovern Institute, Massachusetts Institute of Technology, Cambridge, MA 02139; [b]Harvard–MIT Heath Sciences and Technology Program, Harvard University–Massachusetts Institute of Technology, Cambridge, MA 02139; [c]School of Medicine, Duke University, Durham, NC 27710; [d]Department of Biology, Massachusetts Institute of Technology, Cambridge, MA 02139; [e]Department of Biological and Biomedical Sciences, University of North Carolina at Chapel Hill, Chapel Hill, NC 27599; [f]Department of Brain and Cognitive Sciences, Massachusetts Institute of Technology, Cambridge, MA 02139; [g]Media Lab, Massachusetts Institute of Technology, Cambridge, MA 02139; and [h]Department of Biological Engineering, Massachusetts Institute of Technology, Cambridge, MA 02139

Contributed by Robert Desimone, September 13, 2016 (sent for review March 9, 2016; reviewed by John H. Reynolds, Charles E. Schroeder, and Robert H. Wurtz)

Optogenetic methods have been highly effective for suppressing neural activity and modulating behavior in rodents, but effects have been much smaller in primates, which have much larger brains. Here, we present a suite of technologies to use optogenetics effectively in primates and apply these tools to a classic question in oculomotor control. First, we measured light absorption and heat propagation in vivo, optimized the conditions for using the red-light–shifted halorhodopsin Jaws in primates, and developed a large-volume illuminator to maximize light delivery with minimal heating and tissue displacement. Together, these advances allowed for nearly universal neuronal inactivation across more than 10 mm^3 of the cortex. Using these tools, we demonstrated large behavioral changes (i.e., up to several fold increases in error rate) with relatively low light power densities (≤100 mW/mm^2) in the frontal eye field (FEF). Pharmacological inactivation studies have shown that the FEF is critical for executing saccades to remembered locations. FEF neurons increase their firing rate during the three epochs of the memory-guided saccade task: visual stimulus presentation, the delay interval, and motor preparation. It is unclear from earlier work, however, whether FEF activity during each epoch is necessary for memory-guided saccade execution. By harnessing the temporal specificity of optogenetics, we found that FEF contributes to memory-guided eye movements during every epoch of the memory-guided saccade task (the visual, delay, and motor periods).

primate | optogenetics | FEF | Jaws | memory-guided saccade

The frontal eye field (FEF) is an important brain area for making saccades to remembered locations. FEF neurons increase their firing rate during three epochs of memory-guided saccades: (*i*) target presentation, (*ii*) delay period, and (*iii*) motor preparation. Pharmacological inactivation of the FEF impairs memory-guided saccades (1–7), but because pharmacological inactivation inhibits all FEF neuronal activity, it is unclear if the FEF's role is specific to one or more task epochs (8, 9). By selectively inactivating the FEF during each task epoch, we can determine whether visual-, delay-, or motor-related firing (or some combination of the three types of firing) contributes to memory-guided saccades.

The ideal tool for this study is optogenetics, which allows for millisecond-precise, light-driven neuronal control. Unfortunately, although optogenetics is widely used to study functional physiology and disease models in rodents and invertebrates, technical challenges have limited the use of optogenetics in the nonhuman primate brain, which has a volume ∼100-fold larger than the rodent brain (10). Pioneering studies in monkeys reported small behavioral effects with excitatory (11–14) and inhibitory opsins (15–17). These studies used large light power densities (several hundreds of milliwatts per square meter to 20 W/mm^2) but illuminated only small volumes, at most 1 mm^3, due to both the chosen wavelength and light-delivery method. In contrast, FEF pharmacological inactivation studies report inactivation of volumes of ∼10 mm^3 (2, 3). Further, optogenetically driven neuronal effects in primates are often heterogeneous, decreasing the activity of some neurons and increasing the activity of others (14, 17–19). No primate optogenetics study has reported inactivation levels near the levels of FEF pharmacological inactivation studies, namely, >80% reduction in firing rate relative to baseline reported in >80% of neurons (1–3).

Although many physiological studies have measured the correlation between various neural firing measures and behavior in different brain structures, physiological studies alone cannot establish which neural circuits are critical for which behaviors at any given point in time. Optogenetic methods would seem to be ideal for establishing temporally precise causal relationships, but only if behavioral effects are clear and reliable. Thus, improved methods for establishing larger behavioral effects in primates are a critical need.

Results

We mapped the FEF in two macaque monkeys using microstimulation and electrophysiology. The FEF was defined as the region in the anterior bank of the arcuate sulcus where fixed-vector, saccades were evoked with current <150 μA at least 50% of the time (9, 20–22). Typical thresholds in this study were <50 μA. The receptive field centers were determined based on the end points of evoked saccades (*SI Appendix*, Fig. S1). Achieving perfectly balanced neuronal populations is nearly impossible in the FEF, which is buried in the arcuate sulcus, because electrodes must go down its curved bank along a complex and variable trajectory through layers with unequal distributions of neuronal subtypes (23–25). To mitigate this anatomical limitation, we recorded neurons in these same locations to confirm the presence of target-, delay- and motor-responsive units before recording and quantified the distribution during testing as well. The behavioral paradigm used in this study is shown in Fig. 1. Based on the results of prior pharmacological inactivation studies and our FEF mapping in both monkeys, we

Significance

The frontal eye field (FEF) is critical for making eye movements to remembered locations. FEF neurons increase their firing rate in response to seeing a target, to remembering the target location during a delay period, and to planning eye movements to the location. Conventional tools do not allow us to determine what aspects of FEF neuronal activity (i.e., visual, delay, motor) are critical for memory-guided eye movements, so we developed optogenetic tools to inactivate FEF neurons during each task epoch individually. We found that all aspects of FEF firing contribute to behavior. Further, we present tools that inactivate large enough brain volumes for optogenetics to be widely used in primate neuroscience and, potentially, human medicine.

Author contributions: L.A., E.S.B., and R.D. designed research; L.A. and E.N.P. performed research; E.S.B. contributed new reagents/analytic tools; L.A. and E.N.P. analyzed data; and L.A., E.N.P., E.S.B., and R.D. wrote the paper.

Reviewers: J.H.R., Salk Institute for Biological Studies; C.E.S., Nathan Kline Institute for Psychiatric Research; and R.H.W., National Institutes of Health.

The authors declare no conflict of interest.

[1]To whom correspondence may be addressed. Email: desimone@mit.edu or leah.acker@duke.edu.

This article contains supporting information online at www.pnas.org/lookup/suppl/doi:10.1073/pnas.1610784113/-/DCSupplemental.

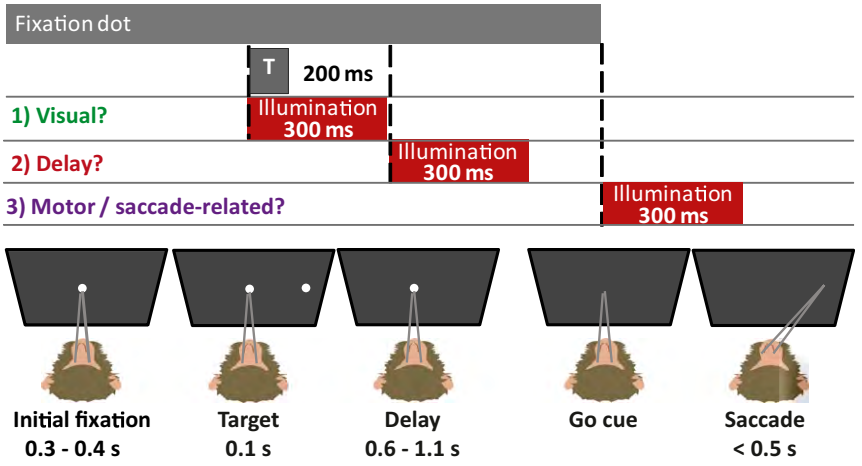

Fig. 1. Memory-guided saccade task with illumination (or sham) at one of three task times (T). After an initial fixation of 300–400 ms (randomly assigned to eliminate timing cues), a target appears for 100 ms in one of the possible target locations (*SI Appendix*, Fig. S13). In a third of trials, a shutter (either the laser shutter or a sham shutter) opens with target presentation and closes 300 ms later to encapsulate all visually related activity in the FEF. In another third of trials, a shutter opens during the delay period, which is randomly distributed from 600 to 1,100 ms to prevent the monkey from using timing cues. In a final third of trials, a shutter opens with the go-cue (i.e., the disappearance of the fixation dot). The monkey has 500 ms to initiate a saccade.

identified the tissue volume needed for opsin expression and illumination (~10 mm^3); the fraction of neurons that, ideally, needed to express the opsin within that volume (>80%); and the firing-rate reduction needed in each neuron (>80%, relative to baseline) for behavioral effects. These parameters guided technological development.

In Vivo Light Propagation. To compare visible light wavelengths accurately, and thus select the optimal opsin for our studies, we developed techniques to measure visible light propagation omnidirectionally in vivo. Previous optogenetic studies have used visible light propagation measurements and tissue properties derived from in vitro or ex vivo specimens (26–32). For example, Azimipour et al. (33) recently published an atlas of optical properties and predicted light distribution in rat brain tissue. Their model was later updated to include information about blood vessels (34), yet all of the data in both reports were derived from 0.5-mm-thick ex vivo slices rather than the intact living brain. Gysbrechts et al. (32) similarly sought to ascertain optical properties of fresh rat brain tissue bathed in cold saline, which also contained deoxygenated hemoglobin and likely diluted the blood present in the sample. Gysbrechts et al. (32) used these optical measurements to estimate light-induced thermal effects, but did not validate their estimates with in vivo measurements. Stujenske et al. (35) performed temperature measurements in vivo to ascertain the effects of green light on neural tissue and found that the temperature increases predicted by models were higher than measured in vivo, underscoring the importance of in vivo measurements.

Oxygenated hemoglobin absorbs far more light than deoxygenated hemoglobin, so even the best ex vivo or in vitro preparation likely underestimates blood-related light absorption (36, 37). This underestimation primarily affects light absorption in the 200- to 600-nm wavelength range (i.e., in all colors other than red) in the living brain. We hypothesized that red light would be less affected by absorption. Specifically, we wanted to know if red light propagates so much farther than other colors of visible light in the living brain that it makes more sense to use Jaws, a red-shifted opsin, at a slightly off-peak wavelength (i.e., 635 nm) than to use Arch/ArchT, a green-light sensitive opsin, at its peak wavelength (i.e., 532 nm).

To answer this question, we measured red (635 nm), green (532 nm), and blue (473 nm) light, for completeness, in the living mouse cortex ($n = 5$, $n = 6$, and $n = 5$ mice, respectively). Blue light is frequently used to drive the popular excitatory opsin, channel rhodopsin-2 (ChR2). We elected to use mice for both light propagation and heating tests because most optogenetics studies are performed in rodents, and because we did not want to risk damaging the cortex of a monkey as we worked to determine the proper parameters.

Photons from all directions can stimulate opsins, but previous studies of visible light propagation simply placed a photodiode below the tissue sample to measure incident light in that plane (26–31). Because such measurement devices do not accept photons at all incident angles, we adapted an isometric, ruby-tipped probe strategy to measure true omnidirectional light flux (*SI Appendix*, Figs. S2 and S3). To use the isometric probe in vivo for shorter visible wavelengths than previously measured (38), we devised calibration and testing methods. When visible light struck the probe's tip, ruby-colored photons were emitted in proportion to the incident light power density and recorded via spectrometer (*SI Appendix*, Fig. S4). To allow direct light power measurements, each probe was calibrated for each color (*SI Appendix*, Fig. S5). A 1.5-mm-diameter, flat-cleaved optical fiber was placed on the surface of the cortex using a custom holder that kept the illuminator aligned with the cortex (*SI Appendix*, Fig. S6), which allowed the probe to advance along a fixed trajectory. This large-diameter fiber served as a planar illuminator along the trajectory, where we took measurements in the center of the fiber beam (*SI Appendix*, Fig. S7). The probe remained in gray matter throughout testing. The ruby-photon emission rate due to incident visible light was measured and converted to light power densities using a probe and color-specific calibrations.

Red light propagated much farther in tissue than either the green or blue light (Fig. 2). At a depth of 1.5 mm, nearly fivefold as much red light remained unabsorbed compared with green light. Furthermore, by fitting the individual data from each mouse, absorption (μ_a) and effective (μ_{eff}) coefficients were determined with SE (least-squares curve fit, $R^2 > 0.95$): 635 nm: $\mu_a = 2.14 \pm 0.15$ cm^{-1}, $\mu_{eff} = 6.61 \pm 0.53$ cm^{-1}; 532 nm: $\mu_a = 13.7 \pm 1.33$ cm^{-1}, $\mu_{eff} = 41.1 \pm 4.04$ cm^{-1}; and 473 nm: $\mu_a = 10.6 \pm 0.486$ cm^{-1}, $\mu_{eff} = 31.8 \pm 1.46$ cm^{-1}. These coefficients can be used for Monte Carlo modeling to predict light propagation in vivo for a variety of illuminators and light source geometries (39–42). Based on the superior light transmission of red light in vivo, we elected to use the red light-sensitive halorhodopsin Jaws (43).

Large-Volume Illuminator. After selecting an opsin, we sought to design an illuminator to address two competing goals: large-volume illumination and minimal penetration damage. Previous attempts to address one of these concerns have come at the expense of the other. Bundles of fibers illuminate larger volumes, but the increased penetration diameter leads to greater tissue and vascular damage, because the damage is proportional to fiber diameter (19, 44–48). Tapered glass fibers reduce penetration damage, but narrowly focus light to tiny illumination areas (<100 μm^2) (13, 49). Here, a 250-μm-diameter plastic optical fiber was tapered to a 70- to 100-μm diameter over a 3- to 5-mm-long tip (Fig. 3 *A* and *C*). Rather than focusing light down along the taper, we etched the core and cladding (Fig. 3*B*) to allow light to escape evenly out from the sides of the tip (*SI Appendix*, Fig. S8), thus distributing light broadly over a large area, similar to the larger fiber bundles yet with minimal penetration damage. Compared with a conventional fiber of the same material and diameter, this illuminator

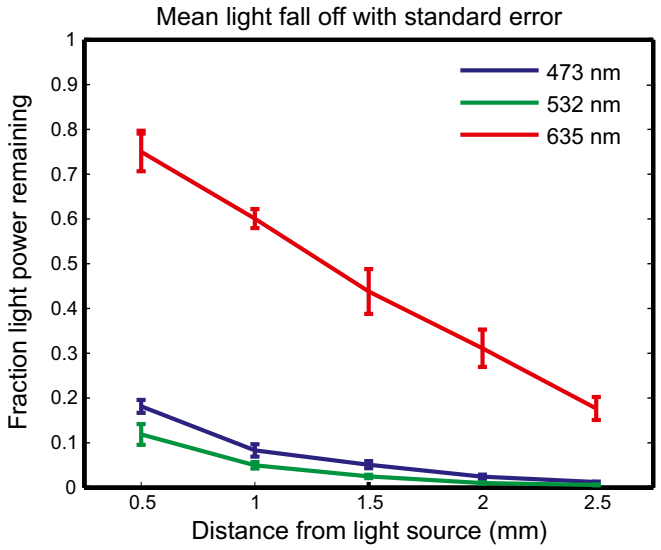

Fig. 2. In vivo measurement of visible light propagation. Average light decrease with distance from the illuminator: mean normalized fluence rates representing the fraction of applied light power reaching a given depth for blue (473 nm), green (532 nm), and red (635 nm) light as a function of distance from the illuminator with SE bars. (For blue, green, and red: $n = 5$, $n = 6$, and $n = 5$ mice, respectively).

has >100-fold the light-emitting surface area and spreads light over >100-fold the tissue volume with equal light power density (*SI Appendix*, Fig. S9). More importantly, however, one can appreciate in a simple photograph that it delivers light more broadly with 1/100th of the light power density in a brain phantom (1.75% agarose) (Fig. 3*E*).

Unlike conventional optical fibers, which must be coupled to an electrode (i.e., an optrode), our illuminator distributes light broadly enough that the illuminator and electrode could be inserted along parallel trajectories 1 mm apart via the same grid used for the virus injections (Fig. 3*F*). Along with reducing penetration damage proportional to diameter, two separate penetrations cause less damage than a single penetration with coupled devices, particularly with 1-mm separation (50, 51) and our illuminator's increased mechanical compliance vs. glass (52). We illustrate light spread of at least 1 mm laterally along the illuminator tip with multicontact electrode recordings from representative neurons (Fig. 3*H*) and local field potential (LFP) optical artifacts (Fig. 3*G*) in monkey L and corresponding data from single-contact recordings in monkey C (*SI Appendix*, Fig. S10).

Tissue Heating. We are aware of two studies that sought to parameterize optical heating in vivo (41, 53), but no previous study has attempted to control the brain tissue heating due to illumination. Temperature increases >4 °C may induce damage, and firing rate increases with a temperature increase of >2 °C in some heat-sensitive brain areas (54–57). Therefore, we sought to control for potential heating in our own experiments by measuring brain temperatures in vivo with our illuminator. Our in vivo brain temperature measurements (*SI Appendix*, Fig. S11) showed >100 mW/mm^2 of 635-nm light could be delivered via the large-volume illuminator 1 mm from the source with <1 °C temperature increase, a commonly accepted conservative limit for changes in brain function (49, 58–60). Preliminary tests showed that temperature increases peaked 1 mm away from the light source (*SI Appendix*, Fig. S12), so the measurements taken here likely reflect the greatest heating in the entire brain and, incidentally, the heating expected for neurons along the electrode trajectory, which was parallel and 1 mm lateral to the illuminator. The maximum total light power density applied in this study was 100 mW/mm^2, similar to what was used in the first electrophysiological demonstrations of optogenetics in the primate (19, 61), as well as to what has been used for optogenetic modulation of superficial cortical neurons through a window on the brain (62, 63). However, it is much lower than subsequent primate studies that reported behavioral changes using maximal light power densities ranging from several hundred milliwatts per square millimeter to >10 W/mm^2 (11–15, 49).

Opsin Expression and Optogenetic Inactivation. We injected an adeno-associated viral vector containing Jaws and a human synapsin promoter (AAV8-hSyn-Jaws-GFP) into regions of FEF where electrical microstimulation evoked saccades with eccentricities of ~10° in both monkeys based on their individual mappings (*SI Appendix*, Fig. S1). Histology from the center of the injection site showed ~90% expression (1,523 of 1,660 neurons) (*SI Appendix*, Fig. S13). We recorded neurons representing all three FEF response profiles (visual-, delay-, and motor-responsive units) (Fig. 4*A*), and the firing rate of nearly every neuron was suppressed (Fig. 4 *B* and *C*). We compared the difference in the firing rate distributions for laser and control trials at equivalent trial times. Of all recorded neurons with visual, delay, or motor activity, 89.6% in monkey L (60 of 67) and 69.2% in monkey C (36 of 52) had a significant decrease in firing rate during the period of illumination. The decrease in firing rate was significant for all subtypes of neurons (visual, delay, and

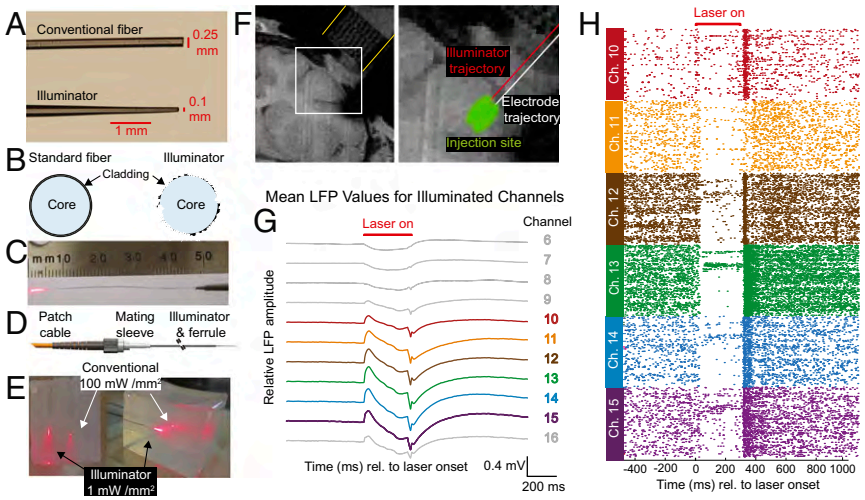

Fig. 3. Illuminator broadly distributes light to inhibit a large volume of primate cortex. (*A*) Illuminator and conventional fiber with the same diameter and material. (*B*) Etched core and cladding spread light broadly. (*C*) Light-emitting, 5-mm-long etched tip. (*D*) Optical fiber/mating sleeve/illuminator interface. (*E*) Illuminator and conventional optical fiber with equal total input light powers in 1-in. cubic brain phantom (1.75% agar). (*F*, *Left*) Coronal MRI from monkey L with a grid in the recording chamber (yellow lines). (*F*, *Right*) Enlarged view with an illuminator and electrode trajectories (1 mm apart), estimated virus injection region, and recording locations. (*F*, *Right*) The width of the chamber outlined with yellow lines is 1 in (25 mm) in diameter. (*F*, *Left*) The electrode and illuminator trajectories shown with red and white lines, respectively, are 1 mm apart. (*G*) LFP light artifact at 0.5-mm–spaced contacts. (*H*) Raster plots of corresponding neurons. For *G* and *H*, $n = 462$ trials.

motor) at all task times (during the target, delay, or go-cue period) regardless of whether or not the target was in the receptive field or opposite to it (Fig. 4*D*). In response histograms averaged for the entire population of cells, the firing rate decreased significantly with illumination ($P < 1e\text{-}10$, t test; $n = 67$ for monkey L and $n = 52$ for monkey C; $\alpha = 0.95$).

As is common with halorhodopsins (64–71), we also observed a small and transient postinhibition "rebound," which was more pronounced in monkey L. The morphology of waveforms was generally consistent before illumination, during illumination, during the rebound, and after the rebound (*SI Appendix*, Fig. S14). To quantify the rebound, the average number of spikes in the 50-ms period from 20 ms after the end of the laser pulse to 70 ms after the end of the laser pulse was measured and averaged across all trials for each condition (including control trials with a sham shutter), neuron, and monkey. For each monkey and neuron, the average firing rate for laser conditions during the delay period was compared with the average firing rate during sham/control conditions. There was a significant difference in firing rate during the rebound period across conditions for 64 of 68 neurons for monkey L ($P < 0.05/68$, t test) and 51 of 79 neurons for monkey C ($P < 0.05/79$, t test). For each neuron, the average number of spikes in the rebound period across conditions for laser and control trials was taken by weighting the per-condition averages by the frequency of each condition and calculating the weighted mean. The average number of spikes during this period in the laser trials was subtracted from the average number of spikes during the rebound period in control trials to yield the average increase in the number of spikes in the rebound period for each neuron. On average, less than one additional spike occurred per trial during the rebound period in both monkeys (monkey L: mean ± SD = 0.965 ± 0.878 spikes per period and monkey C: mean ± SD = 0.350 ± 0.825 spikes per period). The extent of the rebound was not correlated with the extent of silencing in either monkey L ($r = 0.1594$, $P = 0.1942$) or monkey C ($r = -0.0318$, $P = 0.7868$).

For target period illumination in monkey L, the transient rebound firing after the illumination period was followed by elevated firing for up to 400 ms, compared with the control trials (Fig. 4*C*). This elevated firing was measured in a window from 360 to 700 ms after illumination, which encompassed the period after rebound before the randomly timed go-cue on all trials. The firing rate was significantly larger during correct illumination trials compared with correct control trials ($P < 1e\text{-}12$, t test; $\alpha = 0.95$). There was also a small but significant increase for the correct versus incorrect laser trials during this period ($P = 0.018$, t test; $\alpha = 0.95$). Despite these findings in monkey L, there was never a significant difference in the firing rate after rebound for monkey C.

Behavioral Testing. Both monkeys were trained to perform a memory-guided saccade task. After injection and expression, we illuminated FEF neurons to suppress them during specific epochs of the memory-guided saccade task (Fig. 1). Error rates (e.g., failures to execute memory-guided saccades to the proper target location) significantly increased with illumination in both monkeys for targets corresponding to neurons with receptive fields at the site of injection, but not for targets opposite to the site of inactivation (Fig. 5*A*). In both monkeys, error rates increased significantly ($P < 0.05/12$ comparisons, χ^2 analysis) during both the delay and go-cue illumination.

With illumination during the target period, error rates increased significantly in monkey L in the injected receptive field ($P < 1e\text{-}9$, χ^2 analysis) but not opposite to it ($P = 0.38$, χ^2 analysis). In monkey C, there was no significant change in error rate on target illumination trials (injected receptive field: $P = 0.048$, χ^2 analysis; opposite receptive field: $P = 0.81$, χ^2 analysis), but there was a significant increase in saccade latency on correct trials to the target (Fig. 5*D*) ($P = 0.0076$, t test) on those trials. The increase in latency without an increase in errors may derive from a latency/error tradeoff (2).

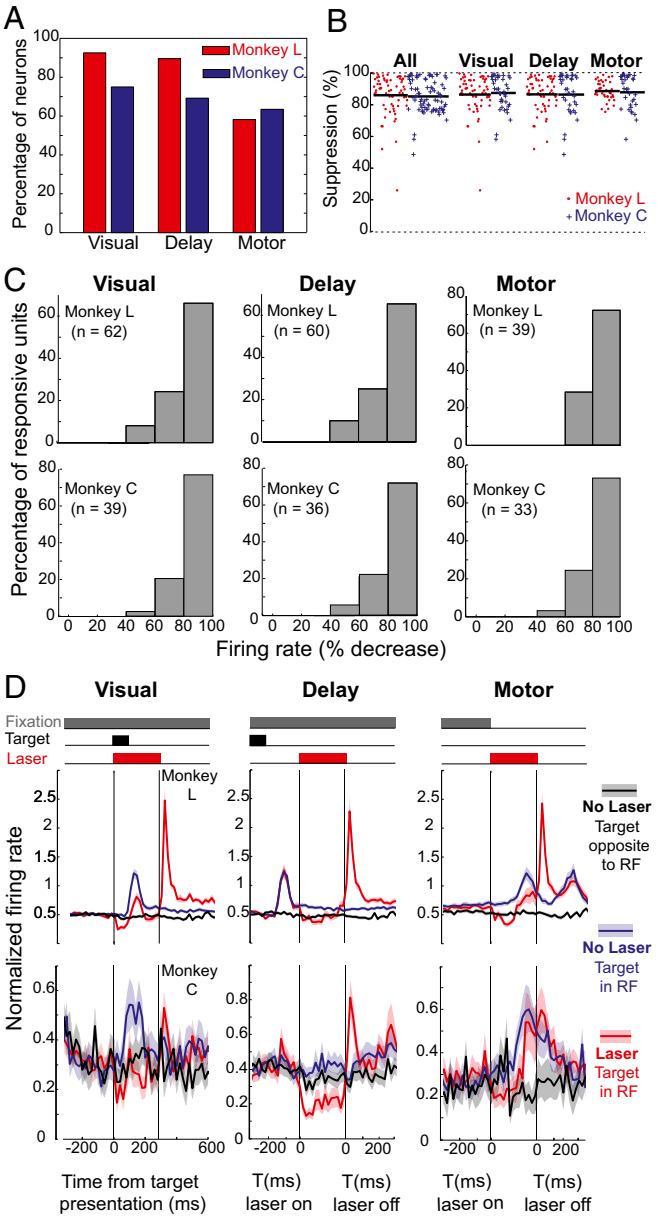

Fig. 4. Nearly universal inactivation of FEF neurons during the memory-guide saccade task dramatically increases error rates to targets in the inhibited receptive field. (*A*) Percentage of recorded FEF neurons with each of the three types of activity in each monkey. (*B*) Percentage of suppression with illumination by subtype with n values. (*C*) Distribution of firing rate decreases for each neuronal subtype in both monkeys. (*D*) Firing profile by subtype. Some neurons shown in *B* for monkey C were not recorded in enough trials for analysis in *C* because to sample more units, single-contact recordings had shorter durations. In monkey C, $n = 19$ (visual), $n = 36$ (delay), and $n = 13$ (motor). In monkey L, n is unchanged. RF, receptive field.

There was also a significant decrease in saccade latency to the opposite hemifield for monkey L with illumination during the target ($P = 0.0007$, t test) and delay ($P = 0.0014$, t test) periods (Fig. 5*D*). Pharmacological FEF inactivation studies reported premature saccades (i.e., correctly targeted saccades initiated before the go-cue) to targets ipsilateral to the injection hemisphere (2). We observed premature saccades in monkey C (Fig. 5*B*) but not in monkey L. Premature saccades were not rewarded despite reaching the proper location. It seems likely that the decreased latency for saccades to the opposite hemifield seen in

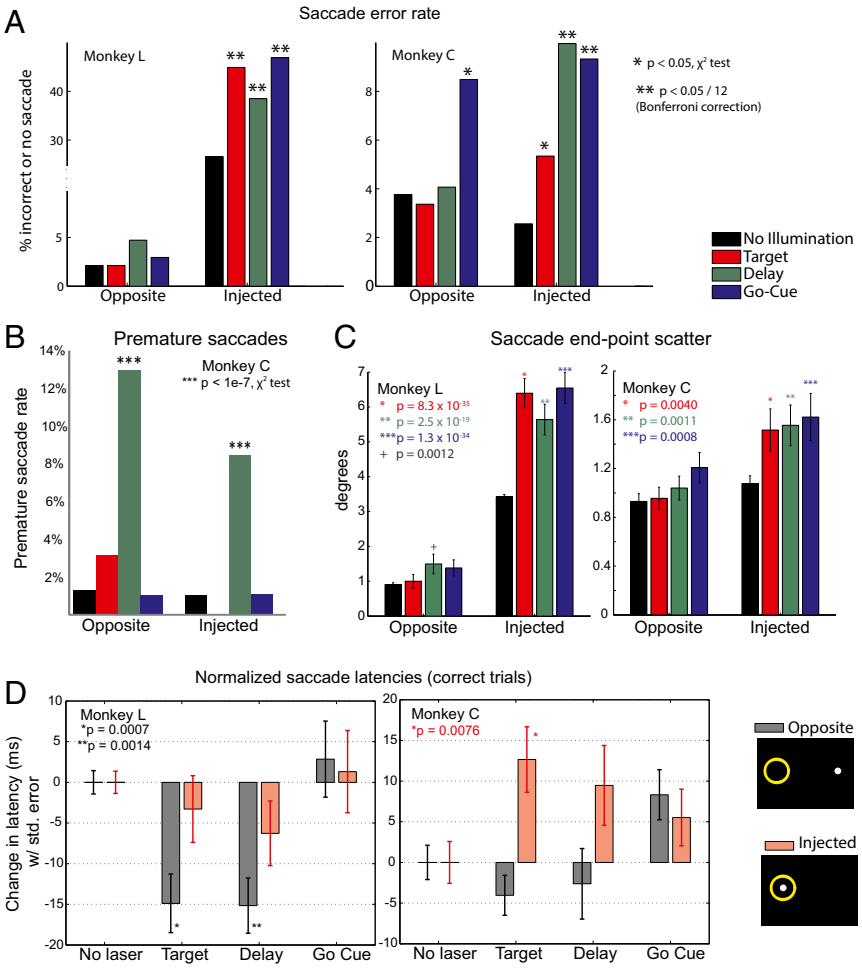

Fig. 5. Optogenetic inactivation significantly increases error rates and alters saccade metrics. (*A*) Error rates increased significantly during delay and motor illumination. During target illumination, behavioral disruptions along the error/latency continuum included increased error rates (monkey L) and increased saccade latency. (*B*) Monkey C made many premature saccades. Data from monkey L are not shown because monkey L did not make any premature saccades. All *n* values are given as the number of premature saccade trials divided by total trials for that condition [no illumination: $n = 9/611$ (Injected), $n = 14/592$ (Opposite); Target: $n = 0/272$, $n = 13/315$; Delay: $n = 29/284$, $n = 58/317$; Go-Cue: $n = 4/287$, $n = 8/290$]. Premature saccades were not rewarded despite reaching the proper location. They likely reflect similar neuronal mechanisms to the decreased latency observed for targets to the opposite side in monkey C. (*C*) End-point scatter significantly increased for targets in the injected receptive field for all illumination conditions in both monkeys, a finding reflecting overall disruption of saccades and consistent with early primate FEF inactivation studies [monkey C: control trials: $n = 409$ (Injected), $n = 403$ (Opposite); Target: $n = 207$, $n = 219$; Delay: $n = 176$, $n = 206$; Go-Cue: $n = 201$, $n = 208$; monkey L: control trials: $n = 1,470$ (Injected), $n = 1,500$ (Opposite); Target: $n = 187$, $n = 174$; Delay: $n = 167$, $n = 153$; Go-Cue: $n = 153$, $n = 160$]. Mean end-point scatter is plotted with SE bars, and uncorrected *P* values (two-tailed Student's *t* test) are shown. (*D*) Average latency for correct nonlaser trials was subtracted from the latencies for correct trials with illumination during the target, delay, or go-cue period for both monkeys to yield the average change in latency, plotted with SE bars [monkey C: control trials: $n = 401$ (Injected), $n = 393$ (Opposite); Target: $n = 175$, $n = 215$; Delay: $n = 193$, $n = 198$; Go-Cue: $n = 214$, $n = 198$; monkey L: control trials: $n = 1,348$ (Injected), $n = 1,466$ (Opposite); Target: $n = 167$, $n = 169$; Delay: $n = 156$, $n = 142$; Go-Cue: $n = 137$, $n = 153$]. Latency significantly increased during the target period for monkey C, which is consistent with the latency/error continuum. The optogenetic behavioral disruption during target presentation, which resulted in an increased error rate in monkey L, manifested itself differently in monkey C, as an increase in the latency of correct trials. As expected, we do not see an increase in the latency of correct trials for conditions where the error rate significantly increased. This figure also shows a significant decrease in saccade latency to the opposite hemifield with illumination for monkey L, a finding manifested as an increased premature saccade rate in monkey C.

monkey L and the premature saccades seen in monkey C are both adaptations to an underlying disruption of saccade control.

Finally, increased saccade end-point scatter has been reported with pharmacological inactivation of the FEF (5) and was also observed with optogenetic inactivation here (Fig. 5*C*). A Student's *t* test was performed comparing scatter for control conditions at a given site with scatter for target, delay, and go-cue illuminated trials at the same site. End-point scatter for targets in the injected receptive field significantly increased for all illumination conditions in both monkeys (Bonferroni correction for 95% significance with 12 comparisons, $P < 0.05/12$). For monkey L, $P = 8.3e\text{-}35$, 2.5e-19, and 1.3e-34, and for monkey C, $P = 0.004$, $P = 0.001$, and 8.5e-4 for target, delay, and go-cue illumination, respectively, on the injected side. There was no significant change in starting point scatter with illumination in either monkey at any condition. Generally, there was no significant increase in scatter to targets on the opposite side, except for a slight increase in scatter with illumination during the delay period for monkey L ($P = 0.0012$). Scatter plots of all saccade end points are shown in *SI Appendix*, Fig. S15.

Discussion

In summary, we obtained large behavioral changes and nearly universal neuronal inactivation over 10 mm^3 of cortex by illuminating 100-fold more tissue at light power densities two- to 100-fold lower than those light power densities previously reported. Behavioral impairments were found during all three phases of the task (target, delay, and saccade periods), suggesting that the FEF makes a contribution to each phase.

The large behavioral changes likely result from several key advances. First, although earlier primate optogenetics studies reported significant firing rate changes in only 38–68% of neurons, all within 400 μm to 1 mm of the light source (14, 18, 19), we found inactivation (>80% firing reduction) over a volume (>10 mm^3) comparable to the inactivated tissue volumes in cooling (1) and pharmacological inactivation studies (2, 3, 7, 72), which silence 80–100% of neurons to <80% of baseline over 4.2–14 mm^3. Second, in contrast with previous studies of inhibitory opsins in primate cortex (14, 18, 19), which report a subpopulation (~10–25% of the total cells) that increases its firing rate during illumination (14, 18, 19) and potentially cancels the effects of inhibition on behavior, not a single neuron in this study increased its firing rate in response to illumination. Optogenetics studies of excitatory opsins have reported similar heterogeneity (17). Finally, we kept heating effects as small as possible, which might have contributed to the heterogeneous neuronal effects in prior studies. This study enables optogenetic silencing to be applied to a wide variety of primate behavior studies and may

also support the application of red-shifted activators, such as Chrimson, for optogenetic activation in primate behavior (73).

Technological Advances. The size of the primate brain has limited the efficacy of primate optogenetics up to this point because most primate neuroscience research, and eventual human translation, requires inactivation of large brain volumes. For example, Ohayon et al. (14) expressed the green-light–sensitive, inhibitory opsin ArchT in the FEF of monkeys and reported no behavior change, no bias of saccadic eye movements, no significant change in saccade direction during combined electrical and optical stimulation, and no change in saccade latency despite 68% of neurons being modulated <1 mm from the light source. Here, the key difference seems to be inactivation of a larger tissue volume (i.e., ∼10 mm, based on our electrophysiological recordings and modeling).

We present an illuminator that, based on our recordings and models, delivers light over 10 mm^3, which is a volume at least an order of magnitude larger than any prior tools with equivalent penetration damage. Further, the tools presented here optimize the wavelength of light, based on actual measurements from the living brain, and control for heating. Previous studies, which used perfused brain preparations or synthetic brain tissue phantoms (53), underestimated tissue absorption for 200–600 nm (blue and green) light propagation. Specifically, we report absorption coefficients two- to threefold larger than the largest reported in a recent study of fresh and frozen brain slices (30) and about 10-fold larger than the values that Yaroslavsky et al. (29) reported based on measurements taken in postmortem human tissue. Unfortunately, the ex vivo values of Yaroslavsky et al. (29) have been used widely in the optogenetics literature (26, 28, 53, 74–78) because, before the present study, techniques were not available for in vivo measurements of light propagation in living brain tissue across the full spectrum of visible light. The absorption coefficient that we determined for red light falls squarely within the range of reported values from extracted tissue and one in vivo study (i.e., $\mu_a = 0.20–4.5\ cm^{-1}$) (29, 30, 79–83).

To limit penetration damage to the FEF, temperature measurements were performed in mice. We assume that heat dissipates more rapidly in primates than in mice due to the larger brain volume over which heat can diffuse, the lower baseline body temperature, and the presence of a large craniotomy through which electrodes and the illuminator are lowered in the monkey. Thus, our heat measurements, if anything, err on the conservative side of overestimation. Vascular densities, impacting light propagation, are similar between mice and monkeys. Estimates of cortical fractional vascular volume (i.e., the fraction of cortex occupied by blood vessels) range from 0. 4–3.6% in mice (84), whereas the average fractional vascular volume in macaque cortex was reported at 2.14%, ranging from 1.93–2.7% across different layers (85). To address the thinner mouse cortex, we stereotactically aligned the light source and the probe so that they both remained in rodent gray matter throughout testing to reflect the cortical primate targets.

Moving beyond the single-area behavioral manipulations shown here, our tools are especially promising for circuit-level optogenetic studies. Inoue et al. (17) evoked saccades with illumination of ChR2-expressing FEF projections in superior colliculus (SC), despite small-volume illumination (<1 mm), large light powers (<1,100 mW/mm^2), and heterogeneous neuronal response (64% excited and 17% inhibited 0.2 mm away from the light source). Even though the saccades in the study by Inoue et al. (17) study were slower, less consistent, and of smaller amplitude than electrically evoked saccades, the demonstration of circuit-level manipulation in combination with the tools presented here opens the door to many new advances in the study of primate neural circuits.

Rebound. We found a rebound in firing rate at the end of the illumination period, which was more pronounced in one of the two monkeys. A recent study suggests that it may be possible to sculpt light pulses (i.e., to ramp down the intensity of illumination over hundreds of milliseconds) to lessen postinhibition rebound firing, if desired The rebound spikes appear to be far fewer than needed to induce a saccade in the FEF, and are even fewer than the briefest FEF microstimulation bias we could find in the literature (86, 87), where 20 ms of 200-Hz microstimulation (four pulses) was required to enhance V4 firing statistically in response to visual stimuli and yet no change in behavior resulted. Thus, it seems unlikely that the rebound played a role in the behavioral effects. In monkey L, the firing rate remained elevated after illumination in the target and delay trials. In monkey C, the postillumination firing rate did not remain elevated beyond the brief rebound. Because this firing rate elevation was only seen in monkey L and did not persist after the trial, it seems likely to be caused by the monkey's attempted compensation for the reduced target response.

Behavioral Effects. The fraction of cells inactivated, the volume of inactivation, and the decrease in firing rate of individual cells are comparable between our transient inactivation and prior pharmacological inactivation, cooling, and lesion studies. Our 300-ms optogenetic inactivation will likely generate different types of errors than inactivation lasting hours or more because, in our experiments, inactivation is too transient for circuit-level compensatory mechanisms to come into play. However, a pharmacological inactivation study by Sommer and Techovik (2) reports an increase in the frequency of no-saccade trials from 9% (before injection of muscimol) to 20% (during injection), which is comparable to the change in our total error rate levels. In monkey C, where the baseline error rate was low, we saw a two- to fourfold increase in errors (a raw increase of 2.78–6.77% incorrect). In monkey L, where the baseline error rate was high even before virus injection, there was a 1.45- to 1.76-fold increase (a raw increase of 11.9–20.3% incorrect). This task was more difficult for monkey L than monkey C even without illumination, which may have affected performance during the optogenetic inactivation. Each animal adopts strategies to maximize reward. With different baseline levels of performance ability, the monkeys may have different levels of behavioral adaptation to optogenetic manipulation.

Further, we observed synergistic effects between error rate and latency, and between latency and premature saccades. A pioneering primate optogenetics study (15) in the superior colliculus noted changes in saccade metrics (latency, velocity, and end points) without behavioral performance changes, implying that these metrics are altered at lower levels of inactivation than are needed to disrupt behavior. Previously, we have not had the means to inactivate with the temporal specificity seen using optogenetics. Now, with slightly different inactivation levels, we can tease apart related behavioral continuums. For example, increased saccade latency and saccade errors form a continuum, with the lowest levels of inactivation increasing latency and the highest levels of inactivation causing errors. Because the optogenetically driven increase in error rate limits the pool of trials available for latency analysis, we did not expect increased latency for conditions in which the error rate increased with illumination, which is what we observed.

Finally, the decreased contralateral saccade latencies in monkey L and the increased premature saccade rate in monkey C may indicate disruption of similar neural mechanisms (i.e., the reciprocal transcallosal FEF projections, through which one FEF inhibits the other), which may underlie both premature saccades and decreased contralateral saccade latencies. Thus, similar to the continuum of increased saccade latency and increased error rate on the injected side, decreased saccade latency and premature saccades on the opposite side may represent another continuum of inactivation-driven effects.

Methods

Animals. All animal procedures were in accordance with the NIH guidelines and were approved by the Massachusetts Institute of Technology Committee

on Animal Care. Two adult, male rhesus monkeys (*Macaca mulatta*) weighing 13–16 kg were used for the behavioral study. Sixteen male C57BL/6J mice (Taconic) aged 8–16 wk were used for light power measurements ($n = 5$ for 473 nm, $n = 6$ for 532 nm, and $n = 5$ for 635 nm).

Implantation. Anatomical MRI was performed preoperatively to determine stereotactic coordinates for chamber placement. All surgical procedures were carried out under anesthesia and aseptic conditions. Intraoperative i.v. antibiotics, fluids, and antiinflammatories, as well as postoperative antibiotics and analgesics, were administered, as needed. A recording well (19-mm inner diameter; Crist Instruments Company) over one FEF and a titanium head post were implanted surgically under aseptic conditions. A craniotomy was made inside the chamber.

MRI. Additional anatomical MRI was performed on each monkey. A custom ultem recoding grid with 1-mm hole spacing was placed in the chamber and filled sterile surgical lubricant (SurgiLube) to allow for grid visualization. A screw on the side of the chamber fit into a notch on one side of the grid to ensure consistent orientation across all imaging, procedures, and testing sessions. MRI was processed offline using software (Amide).

Microstimulation. During awake testing, an *x–y* stage (NAN Instruments) was fixed in a consistent orientation over the recording chamber with the grid. Microdrives (NAN Instruments) were mounted on the *x–y* stage and used for microstimulation; electrophysiological recording; and, later, for in vivo illumination. To locate the FEF precisely within the craniotomy, a 220-μm, parylene-coated, tungsten microelectrode (Nimer Lab; WeSense) was lowered to depths spanning the thickness of cortex through the ultem grid. One grid hole per day was tested. The FEF was defined as the region of cortex in the vicinity of the principal and arcuate sulci, where fixed-vector saccades could be evoked with a current of <150 μA at least 50% of the time. Here, the monkey performed a central fixation task while seated 57 cm in front of a cathode ray tube (CRT) computer monitor (resolution: 1,024 × 768 pixels, refresh rate of 75 Hz). A video-based eye tracking system (Eye Link II; SR Research) tracked eye position (250 Hz). Between trials, electrical stimulation was triggered manually via a digital stimulator (WPI) and stimulus isolation unit (WPI). A train of 100 bipolar pulses was applied with a frequency of 250 Hz and a total pulse width of 0.2 ms (0.1 ms depolarization followed by 0.1 ms hyperpolarization) via the microelectrode. Applied currents ranged from 10–300 μA. Electrical current output was constantly monitored with an oscilloscope. This study specifically sought to find areas of the FEF in which microstimulation evoked visual saccades with eccentricities of ∼10 visual degrees.

Electrophysiology and Data Collection. In monkey C, a single-contact, 220-μm, parylene-coated, tungsten microelectrode (Nimer Lab) was lowered into the cortex with a microdrive through a 25-gauge guide tube that just penetrated the dura. In monkey L, a 16-channel, multisite, linear electrode (U-Probe; Plexon) was used instead of the single-contact electrode to allow for better characterization of neuronal populations with fewer penetrations. The electrode, which was lowered and driven in the same way in both primates, was coupled to a preamplifier (Plexon) via a head stage (Plexon) and an electrical connector (Omnetics). Spikes and LFPs were recorded using a multichannel acquisition processor (MAP) system or MAP box (Plexon). The output from each electrode was passed through a high-impedance head stage and then to a preamplifier, which split the data into spike channels (0.25–8 kHz) sampled at 40 kHz and LFP channels (0.7–170 Hz) sampled at 1 kHz. Preamplifier output went into the MAP box, where it was filtered and acquired using Rasputin (Plexon) software. Spikes were sorted offline using principal component analysis and manual waveform shape analysis (Offline Sorter; Plexon). Eye movements were tracked (EyeLink II) and recorded in parallel (MonkeyLogic; Plexon). Behavior codes generated in MonkeyLogic were a sent to the Plexon software in real-time via strobe codes. MATLAB (MathWorks) was used for further analysis and plotting.

Virus Injection. The grid holes and depths for virus injections were determined for each monkey using microstimulation and recording during a memory-guided saccade task. The injected locations were determined solely by the physiological map of each monkey. Virus injections were performed under general anesthesia. Dexamethasone was administered several hours before virus injection to prevent brain swelling and potentially improve neuronal virus uptake. The grid used during recording and microstimulation was placed in the recording chamber during the injection procedure. Injection syringes (10 μL, gas-tight; Hamilton) were preloaded with 5 μL of sterile silicone oil (Sigma) and mounted on a UMP3 microsyringe injector pump (WPI). To prevent air bubbles, the plunger was depressed until a bubble of silicone oil formed at the tip of the injection needle. Next, aliquots of virus (AAV8-hSyn-Jaws-GFP) were removed from dry ice, quickly thawed on wet ice, diluted 1:10 with sterile PBS (pH 7.4; Life Technologies), centrifuged at 4 °C and 5,000 rpm for 5 min (Beckman Coulter Microfuge 22R Centrifuge, Beckman Coulter, Brea, CA), and loaded into the syringe at a rate of 1 $\mu L \cdot min^{-1}$. To prevent air bubbles, syringes were visually inspected during loading and after loading. Experimenters forced a small amount of virus (∼0.1–0.3 μL) out of the syringe until no more air bubbles were observed in the resulting virus droplet. The virus-loaded syringe was placed in the microsyringe injector pump on a stereotactic arm (Kopf) and aligned such that its trajectory moved directly along the desired grid hole to the target location. In both animals, the deepest site along each trajectory was injected first. The injection needle remained at each injection site for 2 min before it was retracted 0.6 mm to the next injection site. For the last, most superficial injection site along a given trajectory, the injection needle remained in place for at least 20 min before it was removed from the brain. For monkey C, cortical trajectories along two adjacent grid holes were injected. Along one trajectory, 0.8 μL of diluted virus was injected at each of five sites, and along a parallel trajectory 1 mm away, 0.8 μL of diluted virus was injected at each of four sites. For monkey L, trajectories of cortex along three grid holes were injected. Along the first trajectory, 0.4 μL was injected at each of eight sites. The amount of virus per site was reduced to maintain an equivalent total volume of virus across both monkeys. Along the second trajectory, 0.4 μL of virus was injected at each of five sites spaced 0.6 mm apart. Along the third trajectory, 0.4 μL was injected at each of five sites spaced 0.6 mm apart. Recording and testing began 71 d after injection for monkey C and 119 d after injection for monkey L. The delay was longer for monkey L due to scheduling and training issues.

Memory-Guided Saccade Task. Each monkey was seated 57 cm in front of a CRT computer monitor (1,024 × 768 pixels, 75 Hz). The MATLAB-based MonkeyLogic software suite controlled the task and recorded the eye position at 250 Hz using a video-based eye tracking system (Eye Link II). Before each testing session, an eye calibration was performed using the built-in function in the MonkeyLogic software. Both behavior monkeys were trained to perform a memory-guided saccade task (Fig. 1). The trial began with central fixation on a white spot (radius of 0.5 visual degree) for a randomly determined duration of 300–400 ms. Next, while the central fixation spot remained on the screen, a peripheral stimulus (also a white dot with a 0.5-visual degree radius) flashed for 100 ms in one of four (monkey L) or eight (monkey C) predetermined locations, all with an eccentricity of 10 visual degrees (*SI Appendix*, Fig. S16). Target selection for a given trial was random. Both monkeys maintained central fixation during the stimulus flash and for another 500–1,100 ms until the central spot was extinguished. The disappearance of the central spot served as a "go-cue" for the monkey to make a saccade to the remembered location where the stimulus had flashed. Trials with premature saccade initiation were terminated. A juice reward was given for saccades with end points that fell within 3 visual degrees of the flashed stimulus. At one of three possible points in each trial, a shutter (either the laser shutter or an identical "sham" shutter) opened for 300 ms (Fig. 1). In a third of the trials, one of the two shutters opened at the same time as the peripheral cue appeared. In a different third of the trials, one of the shutters opened 200 ms after the peripheral cue disappeared (during the delay period). In the final third of the trials, one of the shutters opened at the same time as the central fixation spot disappeared. The sham shutter was three times as likely to open as the laser shutter to allow enough time between laser trials to prevent tissue heating (i.e., >20-fold pulse duration) and also to improve the morale of the monkeys.

Illumination. The large-volume illuminator was lowered into the brain via a guide tube that penetrated the dura but remained just above the cortex. The electrode and illuminator were lowered into adjacent parallel grid holes located 1 mm apart. Whereas the electrode was lowered via a microdrive, the experimenter inserted the large-volume illuminator into the brain by hand because the illuminator is too flexible to be lowered into the brain by either an electromechanical or screw drive. Both the electrode and large-volume illuminator were retracted via a microdrive. A 635-nm, 500-mW DPSS laser (SLOC) and two identical mechanical shutters (Oz Optics) were controlled via transistor—transistor logic (TTL) pulses from a pulse generator (DS8000; World Precision Instruments, Inc.) with timing controlled by a computer running the MonkeyLogic software package. The laser was coupled to an electrically controlled mechanical shutter via a 200-μm-diameter multimodal optical. The shutter output was coupled to a different 200-μm multimodal diameter optical fiber (ThorLabs) and then to a large-volume illuminator via a ceramic sleeve (Precision Fiber Products, Inc.). Experimenters took several steps to ensure that the monkey could not observe any laser illumination. Any part of the optical fiber that extended into the primate box was shielded with light-absorbing, black electrical tape (3M). All of the hardware that interfaced with the optical fiber was shielded with optically absorbing, black-painted foil (ThorLabs), and

the setup was visually inspected before every testing session. Finally, a bank of five red LEDs (DigiKey) was placed in the testing box and flashed continuously at 2.5 Hz (50% duty cycle), which prevented the monkey's eyes from adjusting to darkness and served as an extra precaution against light leakage.

Analysis. A saccade error occurred when the monkey failed to make a saccade to the correct target. We specifically considered trials in which the monkey maintained fixation until the central spot disappeared. If the monkey failed to move its eyes out of the central fixation window within 500 ms of the go-cue, a "no saccade" error occurred. If the primate attempted to make a saccade but did not move its eyes to the correct target location, an "incorrect" error occurred. If the trials did not end in an error or correct saccade, the monkey either did not initiate the trial or broke fixation at some point during the task. To assess for statistically significant changes in error rates, we used a Pearson's χ^2 test to compare the expected errors for each monkey at each target location (determined from the randomly interleaved sham trials with a shutter but no illumination) with the observed errors for the same monkey at the same target location for all laser times. Specifically, we compared laser vs. no laser conditions in the injected receptive field against each other, and in a separate comparison, we compared laser vs. no laser conditions in the opposite receptive field.

For each neuron, the average firing rate (spikes per second) was calculated during the illumination period in laser trials and during the equivalent time period in control trials. A paired sample Student's *t* test was performed on the average laser and control firing rates for all neurons (or subgroup of neurons) for each monkey. The change in firing rate with illumination was assessed in individual neurons as follows. The number of spikes during the illumination period (or control period) was calculated for each trial in each neuron. The firing rate was normalized based on the location of the target and the period of the trial in which the firing rate was measured (i.e., target vs delay vs. go-cue periods). Specifically, the average firing rate for the target location and task period for control trials was subtracted from the firing rate calculated during the test period for each trial. This difference was divided by the SD of the control trial firing rates for this testing period and target location. The distribution of normalized trial-by-trial firing rates for a given neuron without illumination was compared with the normalized trial-by-trial firing rates for a given neuron during illumination. An *F*-statistic was calculated for each comparison to determine whether the variances were equal at the $\alpha = 0.95$ level, and the appropriate Student's *t* test was applied to the distributions at a 95% confidence level.

Neurons were classified based on whether their firing rate increased at different task times. The firing rate of "visually responsive" neurons increased significantly when a target was presented in the associated receptive field. Specifically, in visually responsive neurons, the firing rate in the period 50 ms to 200 ms after the presentation of the target was significantly higher than the baseline firing rate, 200 ms to 50 ms before target presentation. The firing rate of "delay-responsive" neurons increased significantly during the delay period (relative to the baseline). Specifically, delay-responsive neurons had a significant increase in firing rate for the period 350 ms to 500 ms after the target offset compared with the baseline firing rate (again determined from 200 ms to 50 ms before target presentation). A paired sample Student's *t* test was used once again, with a significance level of 0.95. The firing rate of "motor-responsive" neurons increased during motor preparation. Each neuron was tested for a significant increase in firing at its preferred target location at each task time using a paired sample Student's *t* test at a 95% confidence level. Motor-responsive neurons had a significant increase in the firing rate during the 100-ms window before the start of the saccade. The rate during this motor preparation period was compared with the firing rate calculated for the 100-ms window before the go-cue.

The number of spikes in the 50-ms period from 20 ms after the end of the laser pulse to 70 ms after the end of the laser pulse was measured and averaged across all trials for each condition, neuron, and monkey. This time period was used to exclude silencing while fully encapsulating the rebound for all neurons. The average number of spikes in this period was calculated for control trials that used a sham shutter as well. For each neuron, the average number of spikes in the rebound period across conditions for laser and control trials was taken by weighting the per-condition averages by the frequency of each condition and calculating the weighted mean. The average number of spikes during this period in the laser trials was subtracted from the average number of spikes during the rebound period in control trials to yield the average increase in the number of spikes in the rebound period for each neuron.

Large-Volume Illuminator Fabrication. A 22-gauge wire stripper (StripMaster) was used to remove the polyethylene jacket 15–20 cm from the end of a 250-μm-diameter plastic optical fiber (Industrial Fiber Optics). A table vise clamp (Wilton) was locked onto the stripped end of the fiber while the experimenter held the jacketed end taut parallel to the floor (perpendicular to the vise). The stripped section of the fiber was thinned to a diameter of 60–100 μm using the lower setting of a dual-temperature (570/1,000 F) heat gun (Milwaukee). While still holding the fiber taut, the experimenter removed heat and allowed the fiber to cool, which prevents the fiber from curling. Once the fiber cooled, the experimenter gripped the fiber about an inch to either side of its thinnest point and pulled the fiber apart to create a tapered tip. Although this pulling technique requires some practice, particularly in regulating the heat to prevent the fiber from melting or curling, several members of the laboratory have mastered the technique in less than a day. Next, the tapered tip of the fiber was examined under a 4× dissection microscope (VistaVision). Fibers with forked or curled tips were discarded. To etch the tip to the desired length of light emission and to protect the rest of the fiber during etching, the length of desired light emission (typically 3–7 mm) was measured up from the tip and laboratory tape (VWR) was applied above that level. The exposed tip of the fiber was then uniformly etched on all sides using a 5-μm silicon carbide lapping sheet (ThorLabs) followed by a 3-μm aluminum oxide lapping sheet (ThorLabs). At the other end of the fiber, the 22-gauge wire stripper was used to remove about 5 mm of the jacket. This end was cut flat using a hot knife (Industrial Fiber Optics) and polished to a smooth finish using successively smaller fiber polishing sheets ranging from 5 μm to 0.3 μm (ThorLabs). A fiber microscope (ThorLabs) was used to ensure a smooth and uniform polish. The flat end of the polished fiber was inserted into a stainless steel ferrule with a 260-μm inner diameter (Precision Fiber Products) until it was flush with the coupling end of the ferrule. The fiber was then secured in the ferrule with plastic epoxy (Industrial Fiber Optics). Excess epoxy was removed after 12–24 h of curing. A dust cap (ThorLabs) was placed on the ferrule to protect the fiber. Detailed methods for large-volume illuminator quality control, isometric light probe construction and calibration, and planar illuminator construction are provided in *SI Appendix*.

In Vivo Light Measurements. Before surgery under isoflurane anesthesia, analgesics (buprenorphine, 0.1 mg/kg i.p.; meloxicam, 2 mg/kg i.p.) and an antiinflammatory corticosteroid (dexamethasone, 1 mg/kg i.p.) were administered. A stereotactic, rectangular craniotomy (3 mm medial-lateral × 2.5 mm rostral-caudal) was made in the left parietal bone with the rostral-medial corner 0.5 mm caudal and 0.5 mm lateral to bregma. To keep the cortical surface free from blood, a thin coat of transparent silicone (Kwik-Sil) was placed in a ring around the bony margins of the craniotomy, as needed, to prevent bleeding. The craniotomy was kept moist with saline.

Once the craniotomy surgery was complete, pentobarbital (50 mg/kg i.p.) was administered, and isoflurane anesthesia was removed 3–5 min later, depending on the depth of anesthesia. Mice remained anesthetized in the stereotax and on the heating pad throughout testing. Reflexes were tested regularly to ensure an adequate depth of anesthesia. Supplementary pentobarbital (25 mg/kg i.p.) was administered as needed. Euthanasia was performed at the conclusion of testing. If bleeding onto the surface of the craniotomy was detected either pre- or postexperiment, the animal was excluded from this study.

The planar illuminator was lowered onto the surface of the cortex at the center of the craniotomy using a micromanipulator (Siskiyou). The isometric probe was mounted to a stereotactic holder (Kopf) and lowered from the left at a 28° angle through a channel in the custom aligner (*SI Appendix*, Fig. S6) so that the probe remained in the cortex throughout its trajectory. Ruby fluorescence was monitored in real time during lowering and retraction using the spectrometer and SpectraSuite software. Fluence rates were measured in 0.5-mm increments from 0.5 mm to 2.5 mm beneath the surface of the cortex. At each depth, continuous light pulses were applied via the planar illuminator at five different power densities in the range of calibration. Integration times ranged from 3–3,000 ms, with higher powers requiring shorter integration times. During a single pulse, the spectral output from the light probe was recorded at least 25 times for each applied light power density. The pulse durations ranged from 5 s to 20 s, depending on the integration time needed to avoid saturation. To minimize bleeding, the probe was not retracted until testing concluded. Offline analysis and plotting were performed in MATLAB.

Determining Coefficients from in Vivo Light Measurements. In the photodynamic therapy literature, in vivo light propagation measurements of red and infrared light are made several millimeters away from a small, narrow light source. This paradigm allows for absorption and scattering coefficients to be estimated using simple diffusion theory equations for isotropic point sources. For visible light of sub-red wavelengths, it is not feasible to use point source estimates because too little light reaches these distant points to get accurate measurements. Thus, this work uses a wide, collimated-beam estimate to determine scattering and absorption coefficients. For this work, a planar illuminator was used to approximate a wide, collimated-beam source.

Two manually calibrated spectrometers (Ocean Optics) were used in this study, and their peak ruby wavelengths differed slightly, leading to different ruby wavelength ranges. The ruby wavelength range was 695.7–698 nm for

the older device and 692–695 nm for the newer spectrometer. All tests with a given ruby sphere probe were performed using the same spectrometer that was used for calibration without disconnection. In SpectraSuite, photons were measured across the range of ruby wavelengths. Offline, in MATLAB, the photon count was normalized by the integration time to yield a fluence rate (photons per second). Fluence rates for each condition in each mouse were averaged across all trials at every wavelength (omitting the first trial due to possible software lag). The calibration curve was used to convert the mean fluence rates (photons per second) into light powers (milliwatts). The light power reaching a given depth was divided by the applied light power to yield a normalized fluence rate (or fraction of light power remaining). The normalized fluence rates for all light powers at a given depth in a given mouse were averaged to yield mean normalized fluence as a function of distance from the illuminator for each mouse.

According to diffusion theory, in the limit where μ_a, the absorption coefficient, is much larger than μ_s', the reduced scattering coefficient, a wide-beam collimated irradiance incident on a thick slab with refractive index-matched boundaries, has a fluence rate, $\Phi_t(z)$, dependent on z, the vertical distance from the illumination source to the point measured; μ_{eff}, the effective attenuation coefficient; and μ_t, the total attenuation coefficient (Eq. **1**). Assuming $\mu_a/\mu_s << 1$, no sources deep within tissue, and a semiinfinite medium with isometric scattering, the effective and total attenuation coefficients can be related to one another (Eq. **2**), and subsequently rearranged to solve for the total attenuation coefficient, μ_t (Eq. **3**). Substituting Eq. **1** into Eq. **3** yields Eq. **4**. A full derivation can be found a study by Star (88)

$$\Phi_t(z) = (5/(1+2*\mu_a/\mu_{eff}))*exp(-\mu_{eff}*z) - 2*exp(-\mu_t*z) \quad [1]$$

$$\mu_{eff} \approx sqrt(3*\mu_a*\mu_t) \quad [2]$$

$$\mu_t = \mu_{eff^2}/(3*\mu_a) \quad [3]$$

$$\Phi_t(z) = (5/(1+2*\mu_a/\mu_{eff}))*exp(-\mu_{eff}*z) - 2*exp(-\mu_{eff^2}*z/3/\mu_a) \quad [4]$$

The normalized fluence functions for every mouse were fit to Eq. **4** using a least-squares approach. All available depths were included in the fit for each mouse. All fits had an R^2 value >0.95. From those fits, μ_a and μ_{eff} were determined for every mouse. Those absorption and effective coefficients were then averaged across all mice of a given color to yield the estimated absorption and effective coefficients for a given color.

In Vivo Heating Measurements. Before placing the large-volume illuminator in a primate, it was inserted into a mouse brain longitudinally such that all of the illuminator remained in the cortex. For the in vivo temperature testing of the large-volume illuminator in the anesthetized mouse brain, five stereotaxic craniotomies, each ~0.3 mm in diameter, were made in the bone. The first, through which the illuminator was advanced horizontally, was 2 mm posterior and 0.5 mm lateral to bregma. The next four craniotomies were placed at the following locations relative to bregma in millimeters (posterior, lateral): (1, 1.5), (1, 2.5), (3, 1.5), and (3, 2.5). Four 33-gauge (0.008-in. diameter) T-type minihypodermic needle thermocouples (HYP0-33-1-T-G-60-SMP-M; Omega) were lowered vertically, one thermocouple into each of these craniotomies. Illumination through the skull confirmed the distance from the illuminator to the thermocouples, which were calibrated at the factory and confirmed for relative temperature increases and decreases in a water bath before testing. Therefore, each thermocouple was placed 1 mm from the illuminator surface along its length as the temperature was recorded. The illuminator delivered 50 mW/mm^2 and 100 mW/mm^2 of red (635 nm) light for 1 s, and the temperature of the surrounding tissue was recorded in real time (*SI Appendix*, Fig. S11). The maximum temperature increase recorded on any of the thermocouples was considered the "temperature" increase. Guided by reports in the literature, a temperature increase of >4 °C was set as the threshold for damage (54–57), whereas a change of >2 °C was set as the threshold for possibly inducing changes in the neuronal firing rate, opening transient receptor potential (TRP) channels, or increasing the probability of neurotransmitter release (89–94). To be conservative relative to the literature, we sought to keep the temperature within 1 °C of baseline after a 1-s test pulse, and eventually elected to use only 300-ms pulses in the actual study. To limit penetration damage, temperature measurements were not performed in primates; however, we assume that heat would actually dissipate more rapidly in primates than in mice due to the larger brain volume over which heat can diffuse, the lower baseline body temperature, and the presence of a large craniotomy through which electrodes and the illuminator are lowered. Beyond testing one pulse, we also evaluated the heat relaxation time of brain tissue and noted additive heating effects when lasers pulses were spaced too closely (*SI Appendix*, Fig. S11). By fitting the relaxation traces for the curves, we determined that we needed an interpulse interval of 20-fold the pulse duration to prevent additive heating. In the actual testing, the average time from the start of one trial to the start of the next was about 2 s. With a laser pulse duration of 0.3 s, we determined that we should illuminate no more frequently than once every third trial to avoid heating and weighted the nonlaser and laser conditions accordingly.

ACKNOWLEDGMENTS. We thank A. Chuong for providing AAV8-hSyn-Jaws-GFP; I. Wickersham for assistance with confocal imaging; M. Henninger for providing base code for Monte Carlo models; M. Heard, J. Winkle, and E. DeGennaro for technical support; and A. Graybiel, R. Mark, N. Bichot, H. Zhou, A. Chuong, F. Yoshida, R. Schafer, and B. Gomes for helpful advice and discussion. L.A. acknowledges funding from a National Defense Science and Engineering Graduate fellowship, the National Science Foundation Graduate Research Fellowship Program, and the Friends of the McGovern Institute. E.N.P. was supported by the Harry and Eunice Nohara Undergraduate Research Opportunities Program (UROP) Fund, the Massachusetts Institute of Technology (MIT) Class of 1995 UROP Fund, and the MIT UROP Fund. E.S.B. acknowledges funding from NIH Grant 2R44NS070453-03A1, the Institution of Engineering and Technology Harvey Prize, and the New York Stem Cell Foundation–Robertson Award. R.D. acknowledges funding from NIH Grant EY017292.

1. Chafee MV, Goldman-Rakic PS (2000) Inactivation of parietal and prefrontal cortex reveals interdependence of neural activity during memory-guided saccades. *J Neurophysiol* 83(3):1550–1566.
2. Sommer MA, Tehovnik EJ (1997) Reversible inactivation of macaque frontal eye field. *Exp Brain Res* 116(2):229–249.
3. Tehovnik EJ, Sommer MA (1997) Effective spread and timecourse of neural inactivation caused by lidocaine injection in monkey cerebral cortex. *J Neurosci Methods* 74(1):17–26.
4. Dias EC, Kiesau M, Segraves MA (1995) Acute activation and inactivation of macaque frontal eye field with GABA-related drugs. *J Neurophysiol* 74(6):2744–2748.
5. Dias EC, Segraves MA (1999) Muscimol-induced inactivation of monkey frontal eye field: Effects on visually and memory-guided saccades. *J Neurophysiol* 81(5):2191–2214.
6. Dias EC, Segraves MA (1996) The primate frontal eye field and the generation of saccadic eye movements: Comparison of lesion and acute inactivation/activation studies. *Rev Bras Biol* 56(Su 1, Pt 2):239–255.
7. Martin JH, Ghez C (1999) Pharmacological inactivation in the analysis of the central control of movement. *J Neurosci Methods* 86(2):145–159.
8. Bruce CJ, Goldberg ME (1985) Primate frontal eye fields. I. Single neurons discharging before saccades. *J Neurophysiol* 53(3):603–635.
9. Bruce CJ, Goldberg ME, Bushnell MC, Stanton GB (1985) Primate frontal eye fields. II. Physiological and anatomical correlates of electrically evoked eye movements. *J Neurophysiol* 54(3):714–734.
10. Herculano-Houzel S (2009) The human brain in numbers: A linearly scaled-up primate brain. *Front Hum Neurosci* 3:31.
11. Jazayeri M, Lindbloom-Brown Z, Horwitz GD (2012) Saccadic eye movements evoked by optogenetic activation of primate V1. *Nat Neurosci* 15(10):1368–1370.
12. Gerits A, et al. (2012) Optogenetically induced behavioral and functional network changes in primates. *Curr Biol* 22(18):1722–1726.
13. Dai J, Brooks DI, Sheinberg DL (2014) Optogenetic and electrical microstimulation systematically bias visuospatial choice in primates. *Curr Biol* 24(1):63–69.
14. Ohayon S, Grimaldi P, Schweers N, Tsao DY (2013) Saccade modulation by optical and electrical stimulation in the macaque frontal eye field. *J Neurosci* 33(42):16684–16697.
15. Cavanaugh J, et al. (2012) Optogenetic inactivation modifies monkey visuomotor behavior. *Neuron* 76(5):901–907.
16. Afraz A, Boyden ES, DiCarlo JJ (2015) Optogenetic and pharmacological suppression of spatial clusters of face neurons reveal their causal role in face gender discrimination. *Proc Natl Acad Sci USA* 112(21):6730–6735.
17. Inoue K, Takada M, Matsumoto M (2015) Neuronal and behavioural modulations by pathway-selective optogenetic stimulation of the primate oculomotor system. *Nat Commun* 6:8378.
18. Han X, et al. (2011) A high-light sensitivity optical neural silencer: development and application to optogenetic control of non-human primate cortex. *Front Syst Neurosci* 5:18.
19. Diester I, et al. (2011) An optogenetic toolbox designed for primates. *Nat Neurosci* 14(3):387–397.
20. Moore T, Fallah M (2004) Microstimulation of the frontal eye field and its effects on covert spatial attention. *J Neurophysiol* 91(1):152–162.
21. Maunsell JHR, Treue S (2006) Feature-based attention in visual cortex. *Trends Neurosci* 29(6):317–322.
22. Murphey DK, Maunsell JHR (2008) Electrical microstimulation thresholds for behavioral detection and saccades in monkey frontal eye fields. *Proc Natl Acad Sci USA* 105(20):7315–7320.
23. Segraves MA, Goldberg ME (1987) Functional properties of corticotectal neurons in the monkey's frontal eye field. *J Neurophysiol* 58(6):1387–1419.

24. Stanton GB, Bruce CJ, Goldberg ME (1995) Topography of projections to posterior cortical areas from the macaque frontal eye fields. *J Comp Neurol* 353(2):291–305.
25. Stanton GB, Deng SY, Goldberg ME, McMullen NT (1989) Cytoarchitectural characteristic of the frontal eye fields in macaque monkeys. *J Comp Neurol* 282(3):415–427.
26. Aravanis AM, et al. (2007) An optical neural interface: in vivo control of rodent motor cortex with integrated fiberoptic and optogenetic technology. *J Neural Eng* 4(3): S143–S156.
27. Huber D, et al. (2008) Sparse optical microstimulation in barrel cortex drives learned behaviour in freely moving mice. *Nature* 451(7174):61–64.
28. Yizhar O, Fenno LE, Davidson TJ, Mogri M, Deisseroth K (2011) Optogenetics in neural systems. *Neuron* 71(1):9–34.
29. Yaroslavsky AN, et al. (2002) Optical properties of selected native and coagulated human brain tissues in vitro in the visible and near infrared spectral range. *Phys Med Biol* 47(12):2059–2073.
30. Mesradi M, et al. (2013) Experimental and analytical comparative study of optical coefficient of fresh and frozen rat tissues. *J Biomed Opt* 18(11):117010.
31. Sterenborg HJ, Van Gemert MJC, Kamphorst W, Wolbers JG, Hogervorst W (1989) The spectral dependence of the optical properties of human brain. *Lasers Med Sci* 4(221): 221–227.
32. Gysbrechts B, et al. (2015) Light distribution and thermal effects in the rat brain under optogenetic stimulation. *J Biophotonics* 9(6):576–585.
33. Azimipour M, et al. (2014) Extraction of optical properties and prediction of light distribution in rat brain tissue. *J Biomed Opt* 19(7):75001.
34. Azimipour M, Atry F, Pashaie R (2015) Effect of blood vessels on light distribution in optogenetic stimulation of cortex. *Opt Lett* 40(10):2173–2176.
35. Stujenske JM, Spellman T, Gordon JA (2015) Modeling the spatiotemporal dynamics of light and heat propagation for in vivo optogenetics. *Cell Reports* 12(3):525–534.
36. Eggert HR, Blazek V (1987) Optical properties of human brain tissue, meninges, and brain tumors in the spectral range of 200 to 900 nm. *Neurosurgery* 21(4):459–464.
37. Robles FE, Chowdhury S, Wax A (2010) Assessing hemoglobin concentration using spectroscopic optical coherence tomography for feasibility of tissue diagnostics. *Biomed Opt Express* 1(1):310–317.
38. Bays R, et al. (1997) Three-dimensional optical phantom and its application in photodynamic therapy. *Lasers Surg Med* 21(3):227–234.
39. Flock ST, Patterson MS, Wilson BC, Wyman DR (1989) Monte Carlo modeling of light propagation in highly scattering tissue–I: Model predictions and comparison with diffusion theory. *IEEE Trans Biomed Eng* 36(12):1162–1168.
40. Flock ST, Wilson BC, Patterson MS (1989) Monte Carlo modeling of light propagation in highly scattering tissues–II: Comparison with measurements in phantoms. *IEEE Trans Biomed Eng* 36(12):1169–1173.
41. Wang L, Jacques SL, Zheng L (1995) MCML–Monte Carlo modeling of light transport in multi-layered tissues. *Comput Methods Programs Biomed* 47(2):131–146.
42. Wilson BC, Adam G (1983) A Monte Carlo model for the absorption and flux distributions of light in tissue. *Med Phys* 10(6):824–830.
43. Chuong AS, et al. (2014) Noninvasive optical inhibition with a red-shifted microbial rhodopsin. *Nat Neurosci* 17(8):1123–1129.
44. Tamura K, et al. (2012) A glass-coated tungsten microelectrode enclosing optical fibers for optogenetic exploration in primate deep brain structures. *J Neurosci Methods* 211(1):49–57.
45. Szarowski DH, et al. (2003) Brain responses to micro-machined silicon devices. *Brain Res* 983(1-2):23–35.
46. Thelin J, et al. (2011) Implant size and fixation mode strongly influence tissue reactions in the CNS. *PLoS One* 6(1):e16267.
47. Bjornsson CS, et al. (2006) Effects of insertion conditions on tissue strain and vascular damage during neuroprosthetic device insertion. *J Neural Eng* 3(3):196–207.
48. Sharp AA, Ortega AM, Restrepo D, Curran-Everett D, Gall K (2009) In vivo penetration mechanics and mechanical properties of mouse brain tissue at micrometer scales. *IEEE Trans Biomed Eng* 56(1):45–53.
49. Ozden I, et al. (2013) A coaxial optrode as multifunction write-read probe for optogenetic studies in non-human primates. *J Neurosci Methods* 219(1):142–154.
50. Jaquins-Gerstl A, Michael AC (2009) Comparison of the brain penetration injury associated with microdialysis and voltammetry. *J Neurosci Methods* 183(2):127–135.
51. Lind G, Gällentoft L, Danielsen N, Schouenborg J, Pettersson LME (2012) Multiple implants do not aggravate the tissue reaction in rat brain. *PLoS One* 7(10):e47509.
52. Nguyen JK, et al. (2014) Mechanically-compliant intracortical implants reduce the neuroinflammatory response. *J Neural Eng* 11(5):056014.
53. Bernstein JG, et al. (2008) Prosthetic systems for therapeutic optical activation and silencing of genetically-targeted neurons. *Proc SPIE Int Soc Opt Eng* 6854:68540H.
54. Kiyatkin EA (2007) Physiological and pathological brain hyperthermia. *Prog Brain Res* 162:219–243.
55. Kiyatkin EA (2004) Brain hyperthermia during physiological and pathological conditions: Causes, mechanisms, and functional implications. *Curr Neurovasc Res* 1(1): 77–90.
56. Kiyatkin EA (2005) Brain hyperthermia as physiological and pathological phenomena. *Brain Res Brain Res Rev* 50(1):27–56.
57. Kiyatkin EA, Brown PL (2004) Modulation of physiological brain hyperthermia by environmental temperature and impaired blood outflow in rats. *Physiol Behav* 83(3): 467–474.
58. Andersen P, Moser EI (1995) Brain temperature and hippocampal function. *Hippocampus* 5(6):491–498.
59. Price RR (1999) The AAPM/RSNA physics tutorial for residents. MR imaging safety considerations. Radiological Society of North America. *Radiographics* 19(6): 1641–1651.
60. McAlinden N, et al. (2013) Thermal and optical characterization of micro-LED probes for in vivo optogenetic neural stimulation. *Opt Lett* 38(6):992–994.
61. Han X, et al. (2009) Millisecond-timescale optical control of neural dynamics in the nonhuman primate brain. *Neuron* 62(2):191–198.
62. Ruiz O, et al. (2013) Optogenetics through windows on the brain in the nonhuman primate. *J Neurophysiol* 110(6):1455–1467.
63. Nassi JJ, Avery MC, Cetin AH, Roe AW, Reynolds JH (2015) Optogenetic Activation of Normalization in Alert Macaque Visual Cortex. *Neuron* 86(6):1504–1517.
64. Madisen L, et al. (2012) A toolbox of Cre-dependent optogenetic transgenic mice for light-induced activation and silencing. *Nat Neurosci* 15(5):793–802.
65. Smith KS, Virkud A, Deisseroth K, Graybiel AM (2012) Reversible online control of habitual behavior by optogenetic perturbation of medial prefrontal cortex. *Proc Natl Acad Sci USA* 109(46):18932–18937.
66. Brown MT, et al. (2012) Ventral tegmental area GABA projections pause accumbal cholinergic interneurons to enhance associative learning. *Nature* 492(7429):452–456.
67. Schöne C, Burdakov D (2012) Glutamate and GABA as rapid effectors of hypothalamic "peptidergic" neurons. *Front Behav Neurosci* 6:81.
68. Arrenberg AB, Del Bene F, Baier H (2009) Optical control of zebrafish behavior with halorhodopsin. *Proc Natl Acad Sci USA* 106(42):17968–17973.
69. Tsunematsu T, et al. (2011) Acute optogenetic silencing of orexin/hypocretin neurons induces slow-wave sleep in mice. *J Neurosci* 31(29):10529–10539.
70. Tønnesen J, Sørensen AT, Deisseroth K, Lundberg C, Kokaia M (2009) Optogenetic control of epileptiform activity. *Proc Natl Acad Sci USA* 106(29):12162–12167.
71. Raimondo JV, Kay L, Ellender TJ, Akerman CJ (2012) Optogenetic silencing strategies differ in their effects on inhibitory synaptic transmission. *Nat Neurosci* 15(8): 1102–1104.
72. Dias EC, Compaan DM, Mesulam MM, Segraves MA (1996) Selective disruption of memory-guided saccades with injection of a cholinergic antagonist in the frontal eye field of monkey. *Soc Neurosci* 81(5):2191–2214.
73. Klapoetke NC, et al. (2014) Independent optical excitation of distinct neural populations. *Nat Methods* 11(3):338–346.
74. Gutierrez DV, et al. (2011) Optogenetic control of motor coordination by Gi/o protein-coupled vertebrate rhodopsin in cerebellar Purkinje cells. *J Biol Chem* 286(29): 25848–25858.
75. Kahn I, et al. (2011) Characterization of the functional MRI response temporal linearity via optical control of neocortical pyramidal neurons. *J Neurosci* 31(42): 15086–15091.
76. Han X (2012) Optogenetics in the nonhuman primate. *Prog Brain Res* 196:215–233.
77. Wang J, et al. (2012) Integrated device for combined optical neuromodulation and electrical recording for chronic in vivo applications. *J Neural Eng* 9(1):016001.
78. Osawa S, et al. (2013) Optogenetically induced seizure and the longitudinal hippocampal network dynamics. *PLoS One* 8(4):e60928.
79. Angell-Petersen E, Hirschberg H, Madsen SJ (2007) Determination of fluence rate and temperature distributions in the rat brain; implications for photodynamic therapy. *J Biomed Opt* 12(1):014003.
80. Cheong W-F (1995) Summary of optical properties. *Optical-Thermal Response of Laser-Irradiated Tissue*, eds Welch AJ, van Gemert MJC (Platinum, New York), pp 275–304.
81. Wilson B, Patterson M, Burns D (1986) Effect of photosensitizer concentration in tissue on the penetration depth of photoactivating light. *Lasers Med Sci* 1(4):235–244.
82. Flock ST, Wilson BC, Patterson MS (1987) Total attenuation coefficients and scattering phase functions of tissues and phantom materials at 633 nm. *Med Phys* 14(5):835–841.
83. Sterenborg HJ, Saarnak AE, Frank R, Motamedi M (1996) Evaluation of spectral correction techniques for fluorescence measurements on pigmented lesions in vivo. *J Photochem Photobiol B* 35(3):159–165.
84. Tsai PS, et al. (2009) Correlations of neuronal and microvascular densities in murine cortex revealed by direct counting and colocalization of nuclei and vessels. *J Neurosci* 29(46):14553–14570.
85. Weber B, Keller AL, Reichold J, Logothetis NK (2008) The microvascular system of the striate and extrastriate visual cortex of the macaque. *Cereb Cortex* 18(10):2318–2330.
86. Armstrong KM, Moore T (2007) Rapid enhancement of visual cortical response discriminability by microstimulation of the frontal eye field. *Proc Natl Acad Sci USA* 104(22):9499–9504.
87. Moore T, Armstrong KM (2003) Selective gating of visual signals by microstimulation of frontal cortex. *Nature* 421(6921):370–373.
88. Star WM (2011) Diffusion theory of light transport. *Optical-Thermal Response of Laser-Irradiated Tissue*, eds Welch AJ, van Gemert MJC (Springer, New York), pp 145–202.
89. Volgushev M, et al. (2004) Probability of transmitter release at neocortical synapses at different temperatures. *J Neurophysiol* 92(1):212–220.
90. Burgoon PW, Boulant JA (2001) Temperature-sensitive properties of rat suprachiasmatic nucleus neurons. *Am J Physiol Regul Integr Comp Physiol* 281(3): R706–R715.
91. Guatteo E, et al. (2005) Temperature sensitivity of dopaminergic neurons of the substantia nigra pars compacta: Involvement of transient receptor potential channels. *J Neurophysiol* 94(5):3069–3080.
92. Moran MM, Xu H, Clapham DE (2004) TRP ion channels in the nervous system. *Curr Opin Neurobiol* 14(3):362–369.
93. Story GM, et al. (2003) ANKTM1, a TRP-like channel expressed in nociceptive neurons, is activated by cold temperatures. *Cell* 112(6):819–829.
94. Xu H, et al. (2002) TRPV3 is a calcium-permeable temperature-sensitive cation channel. *Nature* 418(6894):181–186.

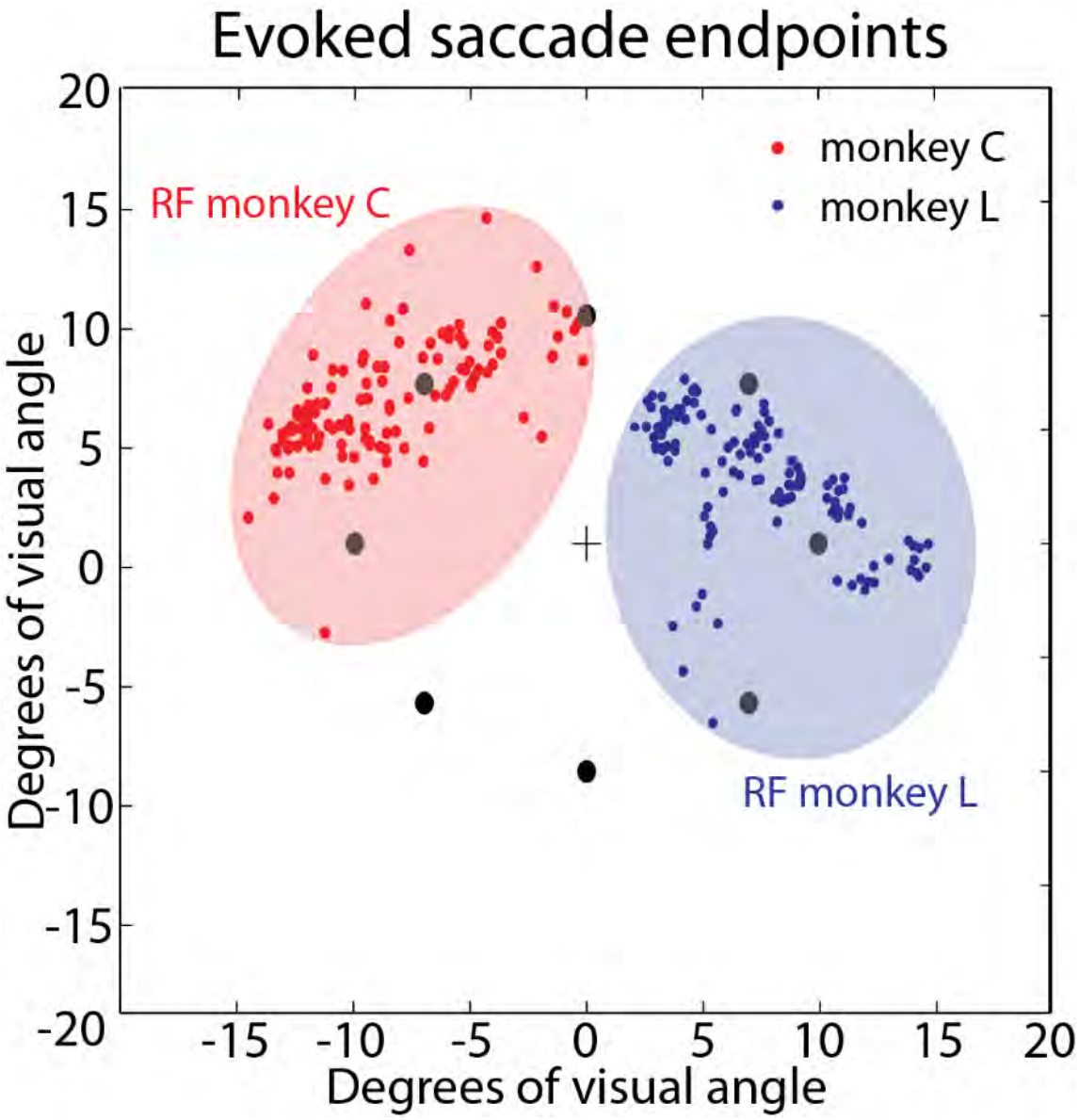

Supplementary Figure 1. Receptive fields evoked in both monkeys

End points of saccades evoked using micro-stimulation in the injection sites in both monkeys with 0.25mm depth spacing (see Online Methods). All end points are relative to a saccade that started in the central fixation location (0, 0) denoted with the cross. The possible target locations, each with an eccentricity of 10° are shown as black circles. The general receptive fields (RFs) for both monkeys are circled and shaded in red (Monkey C) or blue (Monkey L).

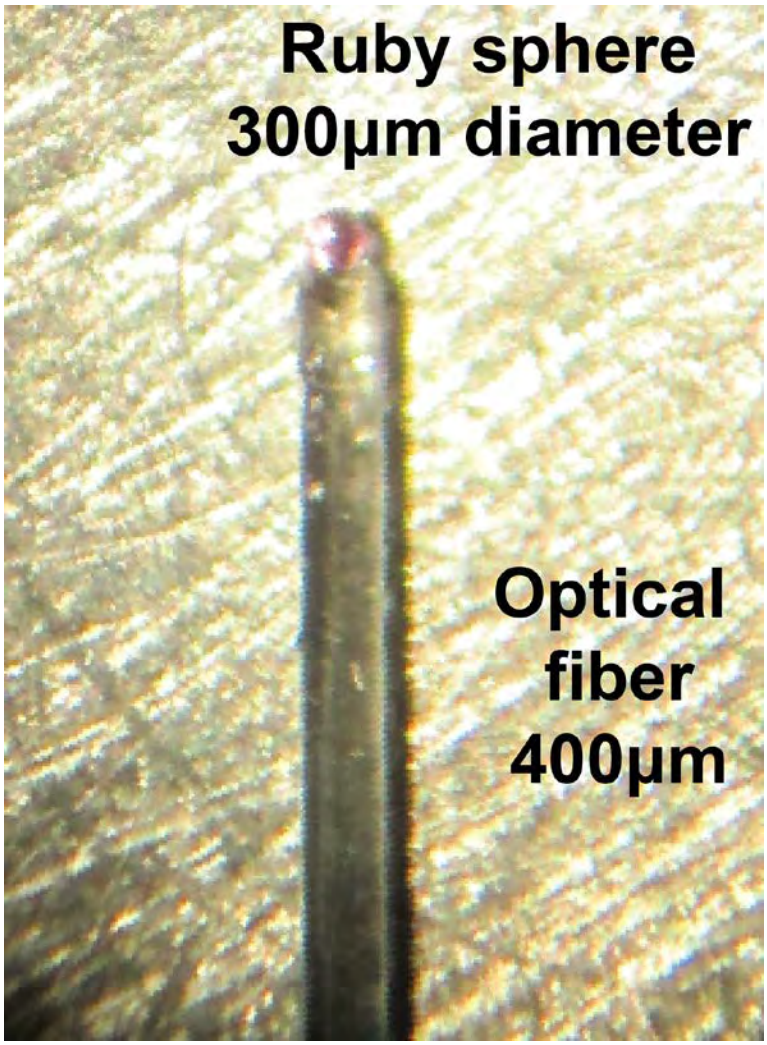

Supplementary Figure 2. Isometric ruby-tipped light probe
Isometric, ruby-tipped light probes were constructed by affixing a 300 µm diameter spherical ruby ball lens (NT46-223, Edmund Optics) to the flat-cleaved, polished end of a 400 µm diameter multimode optical fiber (ThorLabs, BFH48-400, NA = 0.48) with optically-transparent, UV curable adhesive (NT37-322, Edmund Optics). When photons of applied light struck this probe, the ruby tip emitted photons in a random direction independent of the incident photon direction. Measurement of these emitted photons allows for isometric light power measurements.

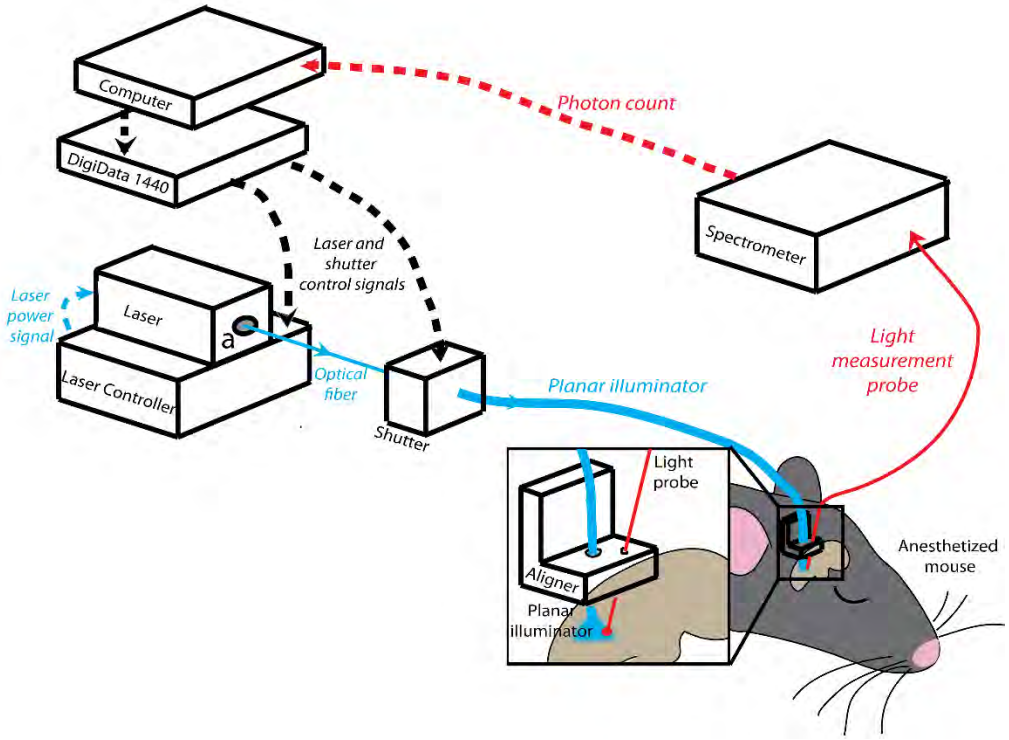

Supplementary Figure 3. A strategy for *in vivo* measurement of visible light propagation.
a) Set up for *in vivo* light measurements with isometric light probe. **b)** Average light decrease with distance from the illuminator: Mean normalized fluence rates representing the fraction of applied light power reaching a given depth for blue (473 nm), green (532 nm) and red (635 nm) light as a function of distance from the illuminator with standard error bars. (n = 5 mice for 473 nm; n = 6 mice for 532 nm; and n = 5 mice for 635 nm).

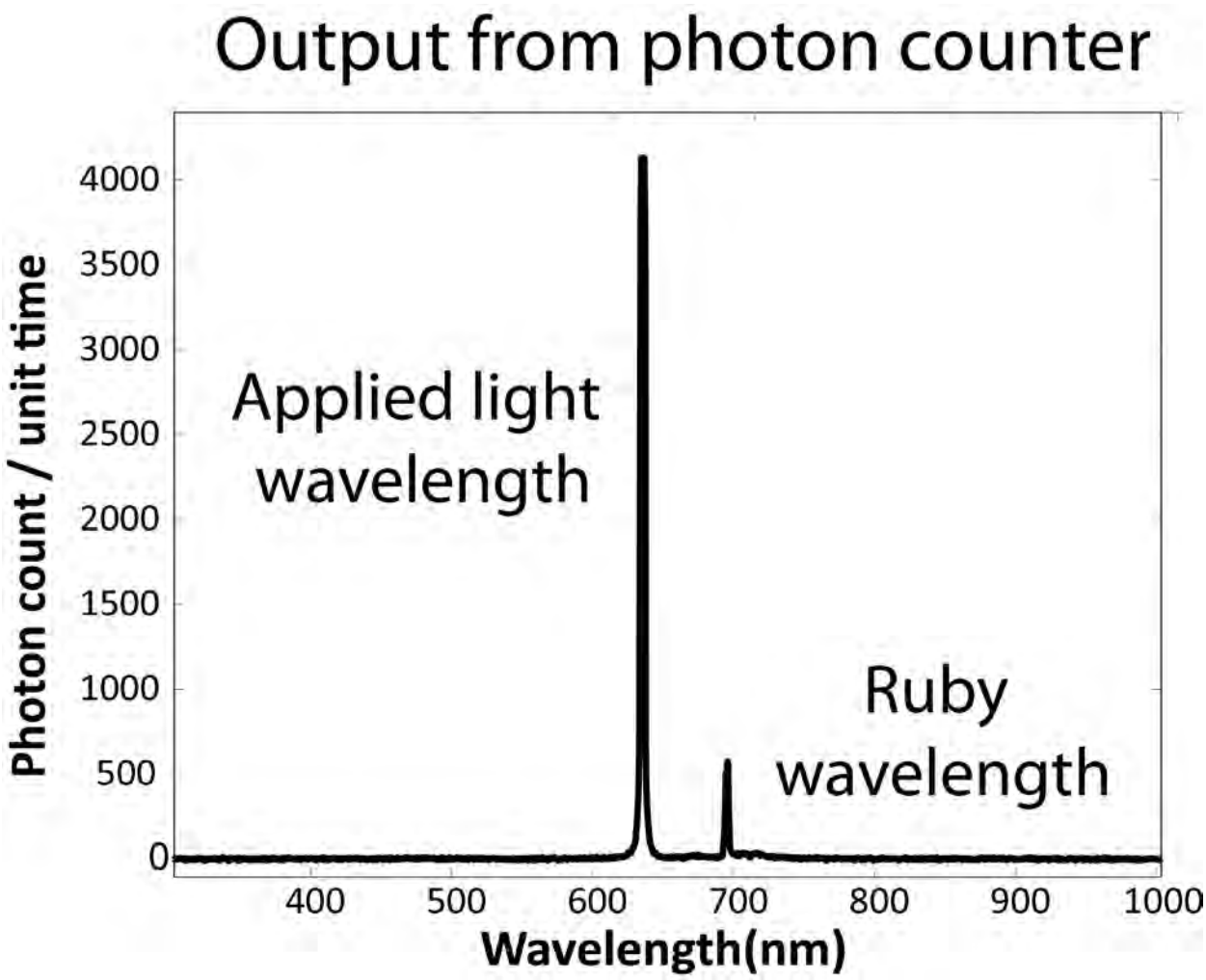

Supplementary Figure 4. Photon count from an isometric ruby-tipped light probe output
Sample spectrometer measurement of the photon count from an isometric ruby tipped light probe shows two peaks. The first peak (635 nm) is an artifact from applied light that struck the probe somewhere other than the tip. The second peak, which is used for light power measurements, reflects the ruby fluorescence induced by the incident light at the tip.

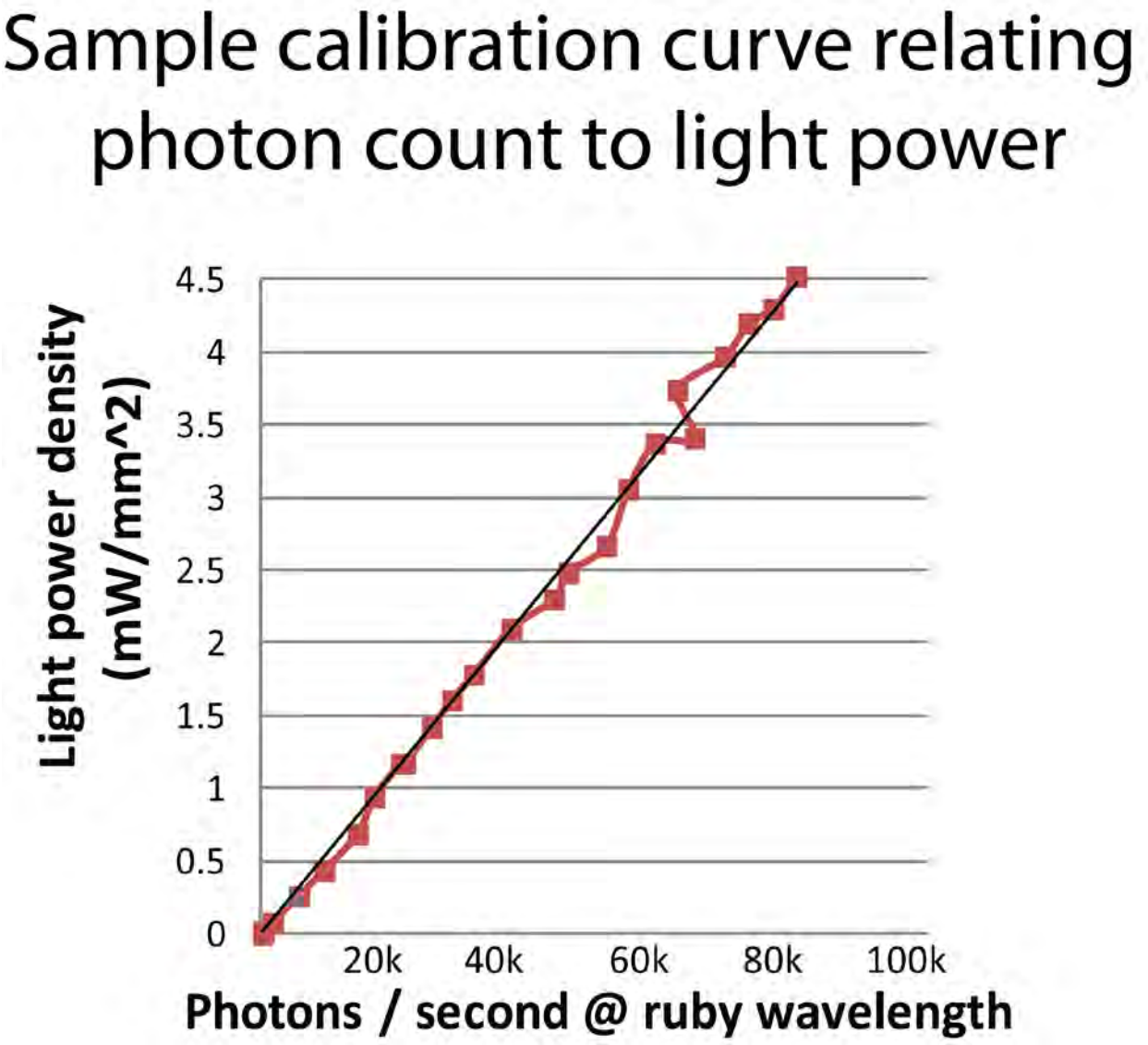

Supplementary Figure 5. Isometric ruby-tipped light probe calibration
An example calibration curve for a isometric ruby-tipped light probe is shown. Light power densities of 0.25 to 4.5 mW /mm^2 were applied to each probe in 0.25 mW /mm^2 increments. The rate of ruby photon emission was measured for each of these applied light power densities and light power density was plotted as a linear function of the ruby photon emission rate. The slope of the calibration curve was then used to relate photon counts measured in vivo to the incident light power density. The intercept for the curve was fixed at 0 because the spectrometer was "dark-corrected" prior to each recording session such that no incident light yielded a photon count of 0.

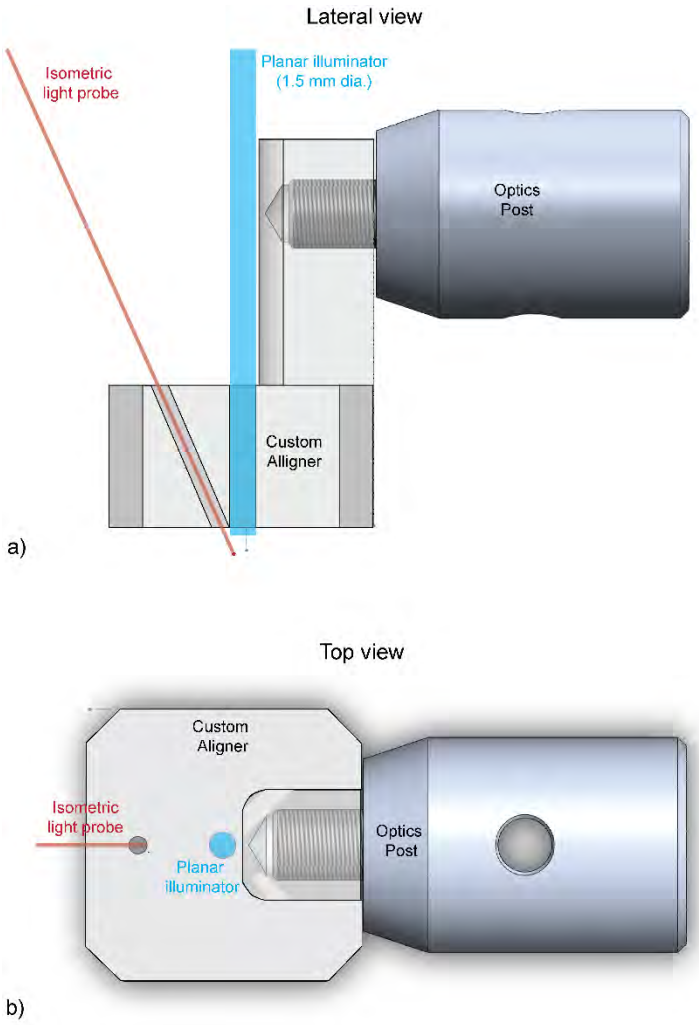

Supplementary Figure 6. Custom aligner for *in vivo* light measurements
(A) The large diameter optic fiber (labeled as “planar illuminator”) was affixed in the center of a 3D printed custom aligner. The isometric ruby-tipped light probe was lowed through a trajectory formed in the custom aligner at a 28 degree angle. This custom aligner interfaced with an optical post (ThorLabs) and was stereotactically lowered on to the surface of the mouse brain. (B) The custom aligner is shown from the side. Additional holes were present, but not used.

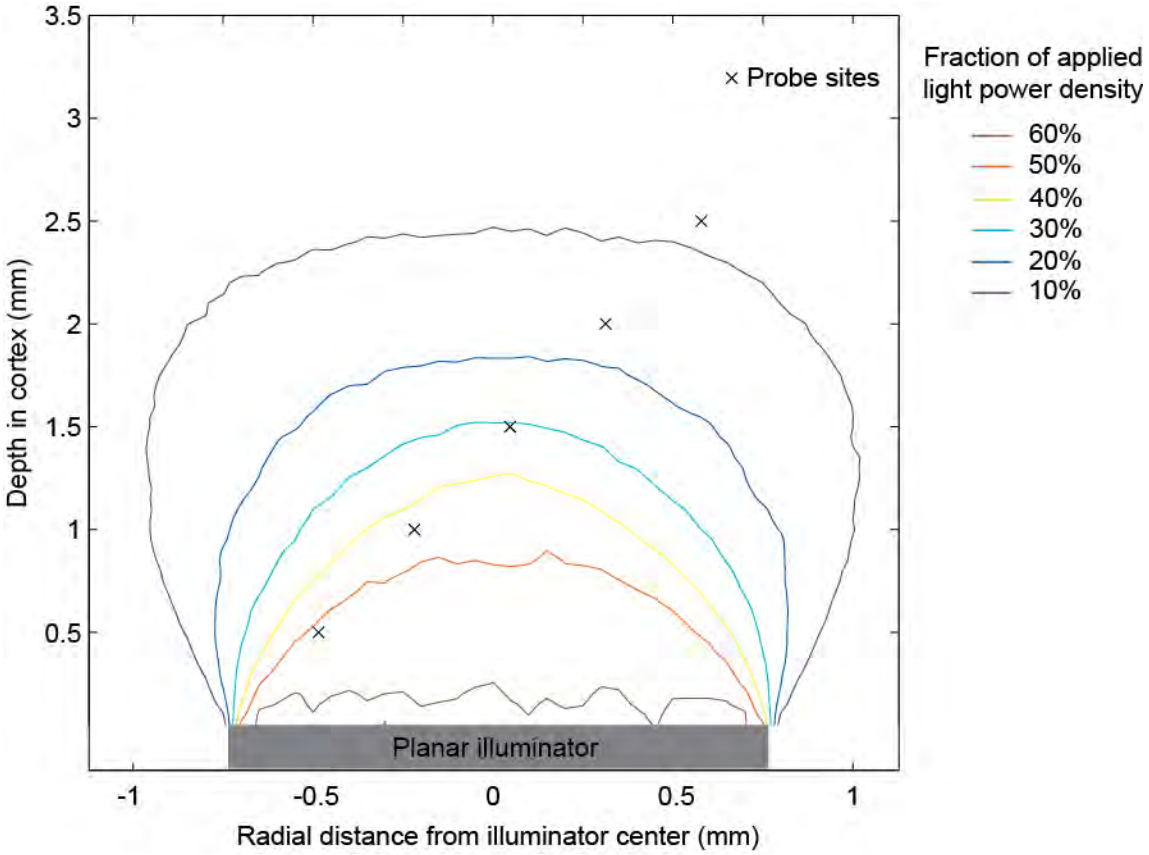

Supplementary Figure 7: Monte Carlo Model of the planar illuminator

Monte Carlo model demonstrates that the planar illuminator light distribution is even over the areas that we illuminate with respect to the illuminator axis. Thus, at each depth, our probe sees the same intensity that it would if it were directly under the center of the illuminator

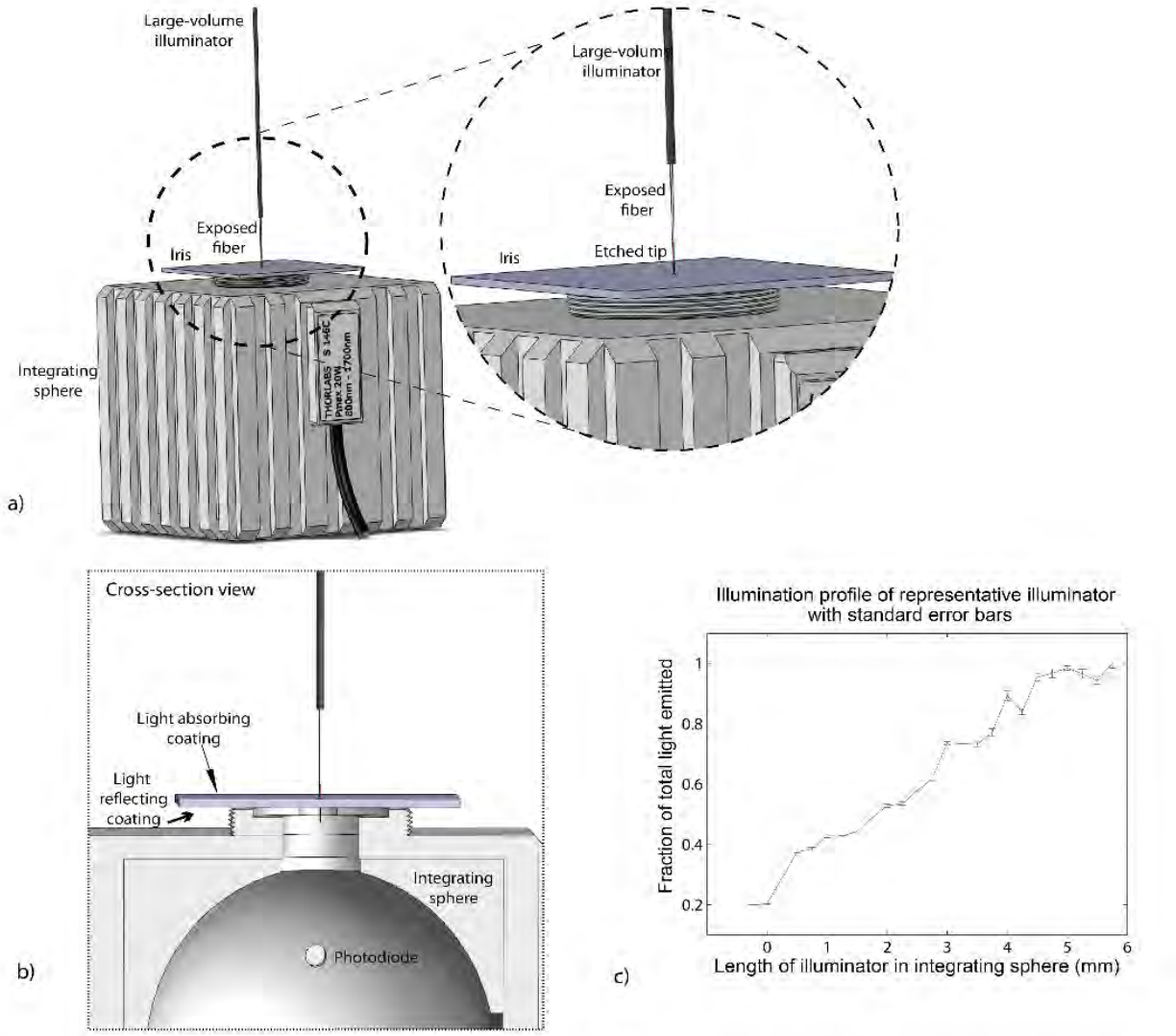

Supplementary Figure 8. Large-volume illuminator calibration

(A) External view of large volume illuminator as it is lower into an integrating sphere covered with a custom iris, such that light emitted above the iris is absorbed and light emitted below the iris is reflected into the sphere for measurement. (B) Cross-sectional view of illuminator profiling set up. (C) Representative illuminator profile with the fraction of total light emission measured as a function of the length of the illuminator that is in the integrating sphere to be measured. An even light emitting surface is critical for the prevention of "hot spots." Specifically, only a small amount (<25%) of total light is emitted at the tip. This calibration ensured that each large volume illuminator distributed light evenly over a large volume.

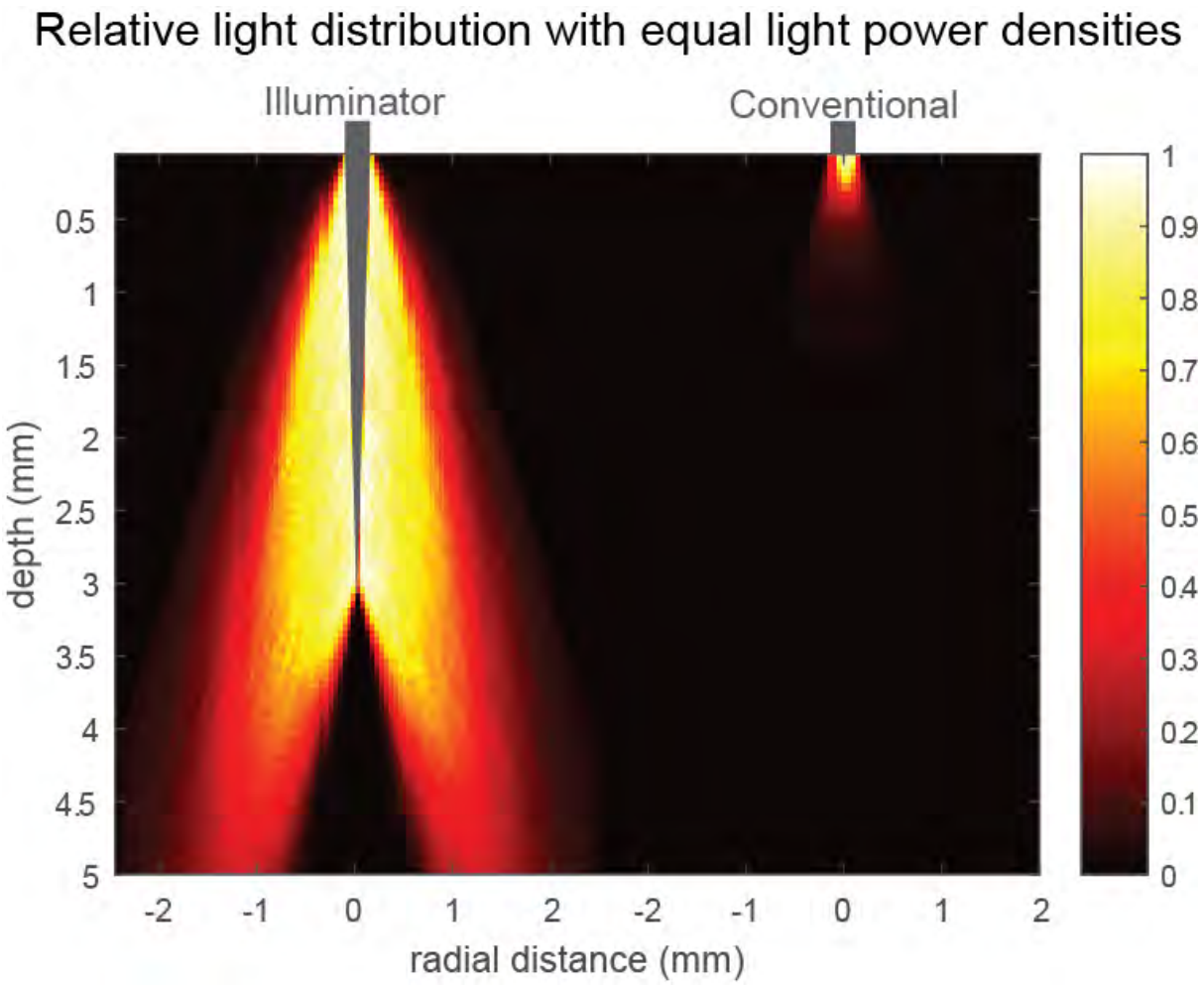

Supplementary Figure 9: Monte Carlo model
Side-by-side Monte Carlo models of a middle cross section of the illuminator (with 3 mm tip length) and a conventional flat-cleaved optical fiber withequal light power densities on their respective surfaces. These 2D models show what the recorded neurons lateral to, and below, the illuminator would see. The 3D profile shapes observed in the brain phantom in **Fig. 3** would result from rotation of these profiles along the axis of the illuminator to yield a 3D representation.

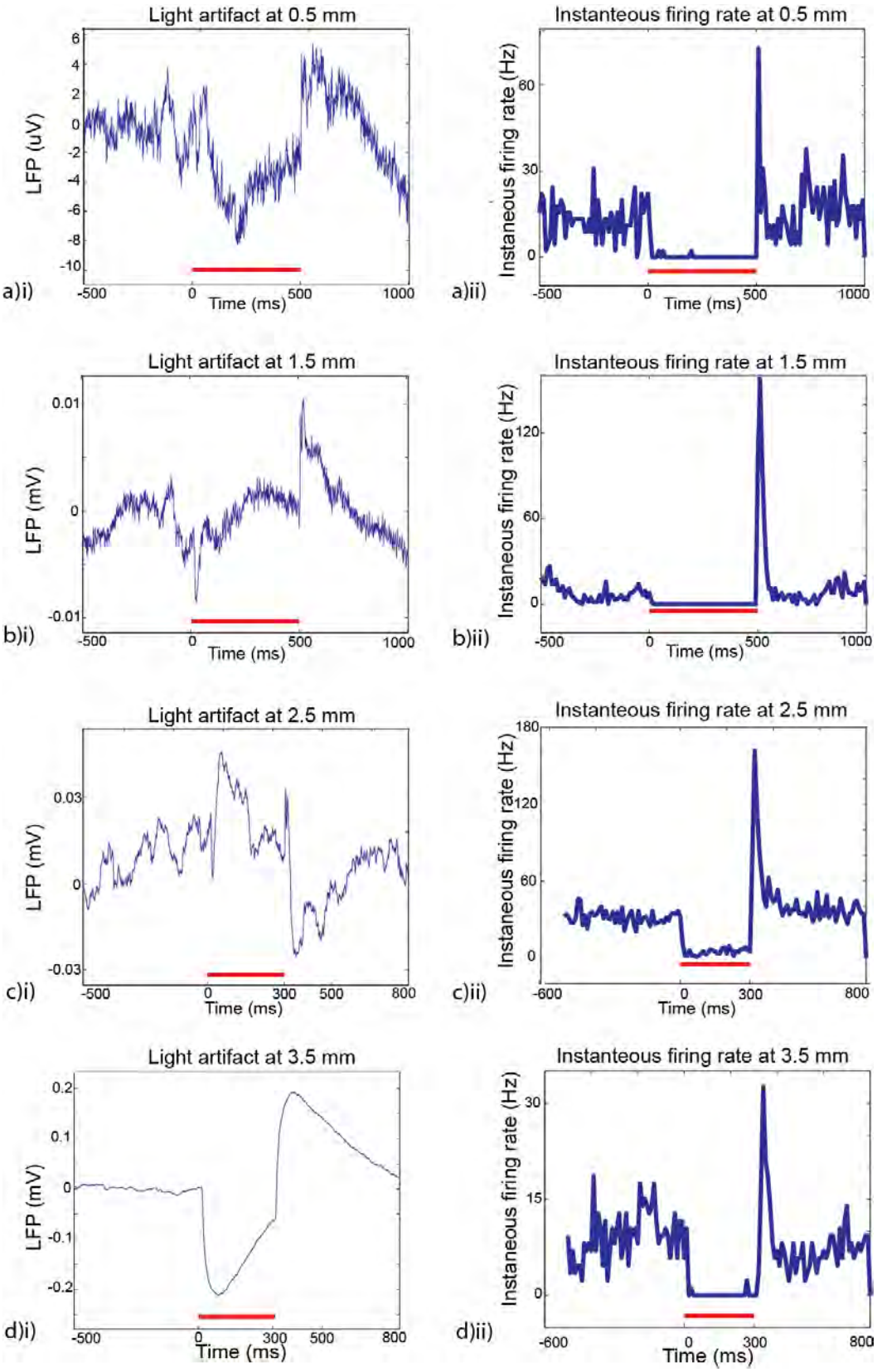
Light artifact at 0.5 mm
LFP (uV)
Time (ms)
a)i)
Instanteous firing rate at 0.5 mm
Instaneous firing rate (Hz)
Time (ms)
a)ii)
Light artifact at 1.5 mm
LFP (mV)
Time (ms)
b)i)
Instanteous firing rate at 1.5 mm
Instaneous firing rate (Hz)
Time (ms)
b)ii)
Light artifact at 2.5 mm
LFP (mV)
Time (ms)
c)i)
Instanteous firing rate at 2.5 mm
Instaneous firing rate (Hz)
Time (ms)
c)ii)
Light artifact at 3.5 mm
LFP (mV)
Time (ms)
d)i)
Instanteous firing rate at 3.5 mm
Instaneous firing rate (Hz)
Time (ms)
d)ii)

S. Fig. 10

Supplementary Figure 10. LFP changes with illumination in monkey C

Local field potential recordings of representative neurons along the injection trajectory of monkey C (left column) and instantaneous spike time histograms at the same locations (right column). The red bar denotes when the laser is on. Note that the virus injections were performed at depths of 0.6 mm relative to the surface of cortex to 3.5 mm relative to the surface of cortex in 0.6 mm intervals. All of this data comes from single contact recordings in Subject C. The shape of the light artifact shown here differs from what was observed Fig. 2g, likely due, at least in part, to electrode differences: u-probe in **Fig. 2g** and a single contact parylene-coated tungsten microelectrode here.

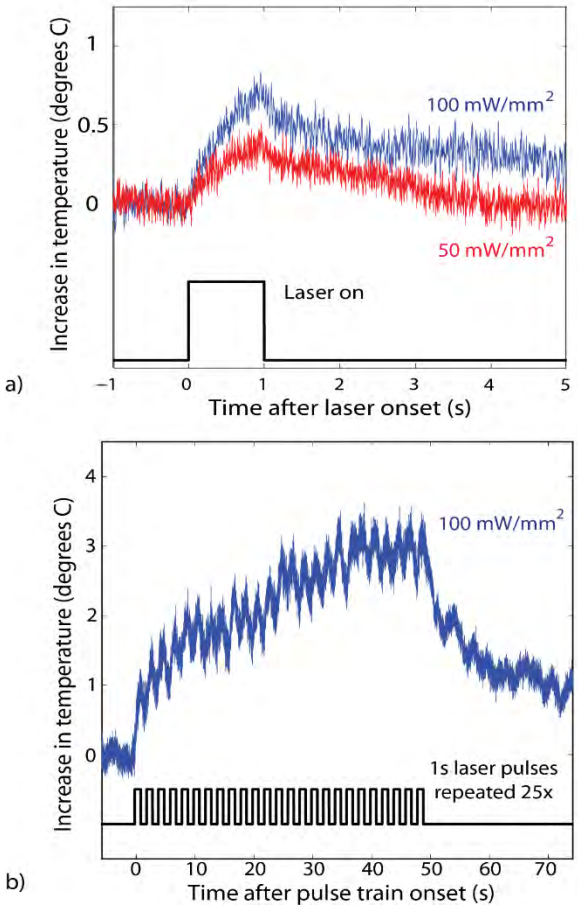

Supplementary Figure 11*. In vivo* temperature measurements with large-volume illuminator
a) Real-time temperature measurements for 1 second 50 mW/mm^2 and 100 mW/mm^2 red (635 nm) light pulses delivered via a large volume illuminator in mouse cortex. Four probes were placed along the illuminator and the probe with the maximum increase relative to baseline is shown. **b)** The heat relaxation time of brain tissue was measured as a train of 1s pulses was applied in the same preparation described above. By fitting the relaxation traces for the curves, we determined that we needed to wait 20 times the pulse duration to prevent any additive heating. In the actual testing, the average time from the start of one trial to the start of the next was about 2 s. With a laser pulse duration of 0.3 s, we determined that we should illuminate no more frequently than once every third trial to avoid heating and weighted the non-laser and laser conditions accordingly.

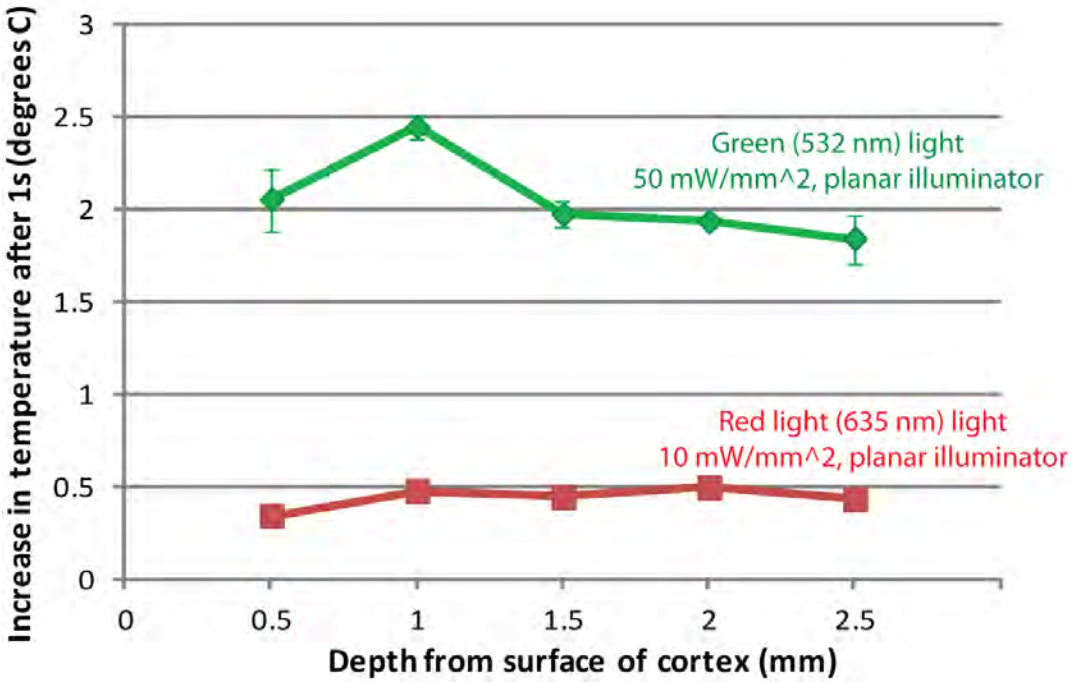

Supplementary Figure 12: Heat measurements at various distances from light source.
In vivo measurements of tissue heating with a large diameter planar illuminator showing that the temperature increase peaks at 1 mm from the light source. **N = 5 mice for each trace.**

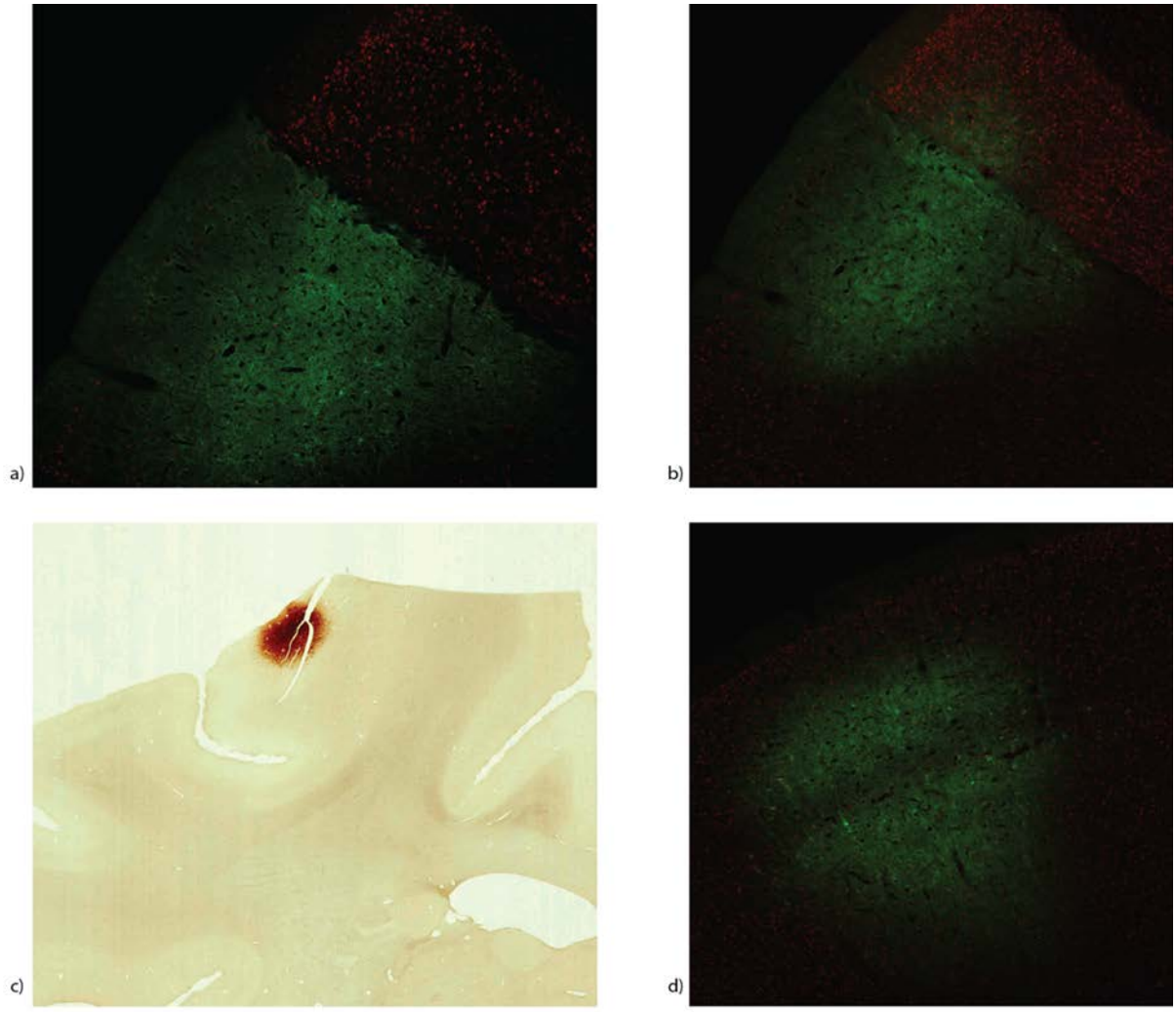

Supplementary Figure 13. AAV8-hSyn-Jaws-GFP expression in macaque FEF

a) AAV8-hSyn-Jaws_GFP expression in macaque FEF. 2 µm thick confocal image of macaque FEF (Monkey R) that was injected with 0.8 µL of AAV8-hSyn-Jaws-GFP diluted to a titer of 6 x 10^{11} particles / mL. at each of four sites spaced 0.6 mm apart in FEF using the techniques described in the methods. The image shows the injected area clearly (including needle tract on the far left side of the image) and tissue in which there was no expression. The similar cell densities in both tissues imply that viral expression did not impact cell health. Neurons are stained in red with NeuN while GFP expression is show in green. In the injected gyrus, 1523/1660 neurons (91.7%) stained green as well, indicating GFP co-expression and viral infection. The sharp line delineating the two regions is the result of a post-perfusion crack in the tissue, illustrated in a DAB stained section from the same region b). b) DAB stained section from the same region imaged with a light microscope. c) Composite image of the entire 50 µm thick section encompassing a). d) section from a site about 1 mm distal to the center of the injection site is shown in a)-c)

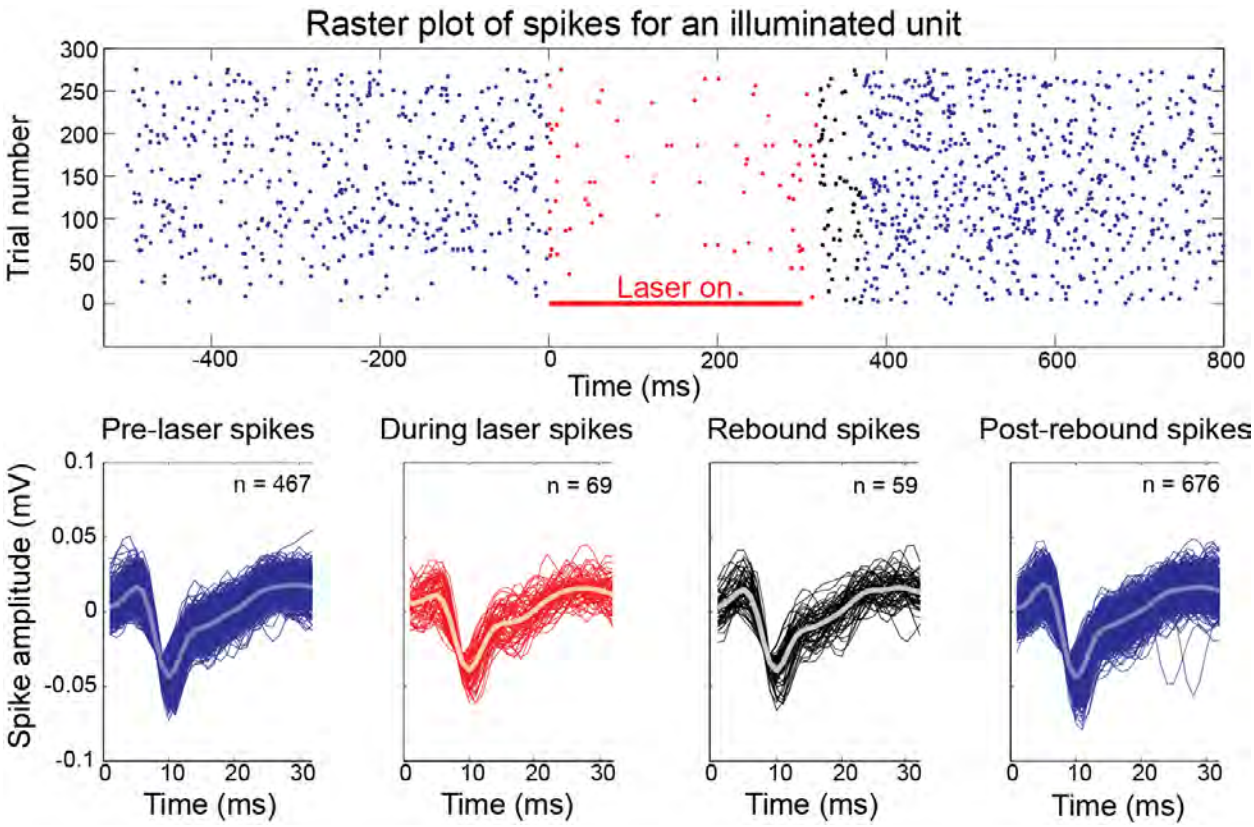

Supplementary Figure 14. Sample waveform.
The top panel shows the raster plot of all illuminated trials for a sample unit. Each dot represents a single spike. In the four panels below are the waveforms for each spike. From left to right, the panels represent pre-illumination spikes, spikes during illumination, spikes during the rebound, and spikes in the post-rebound period. The average spike waveform for each epoch is shown as the lighter colored overlay in the bottom panels. The waveform retains essentially the same shape throughout, though the amplitude is smaller for the spikes during illumination and immediately after during the rebound period.

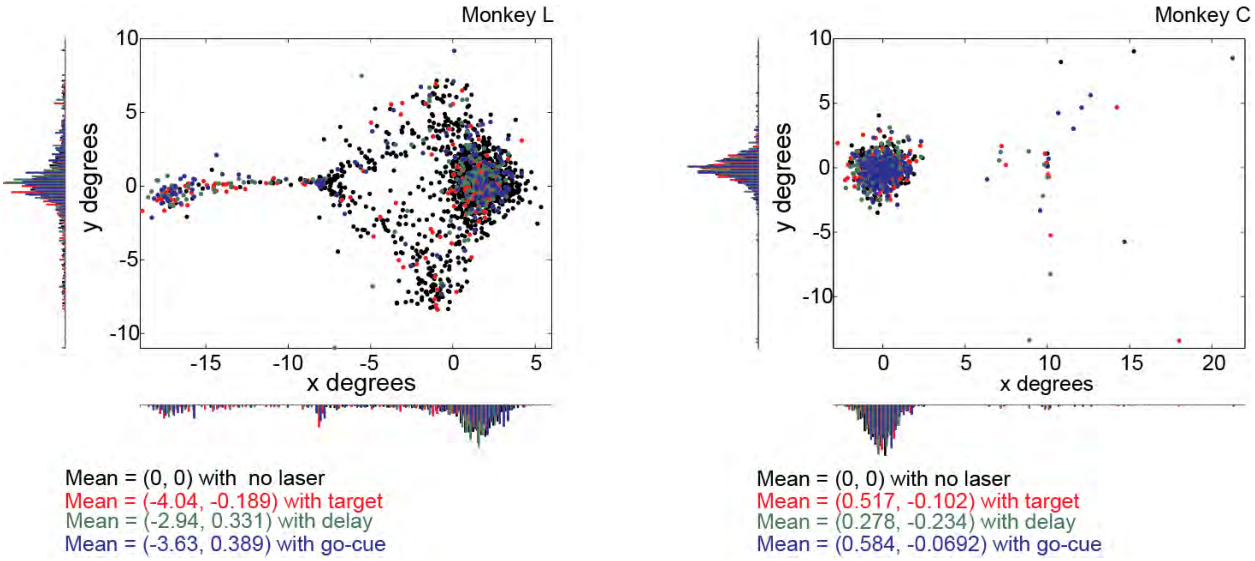

Supplementary Figure 15. Scatter plots of saccade end points

Saccade end points (normalized to the average of the no laser trial end points) for both monkeys for all trials in which a saccade was executed (correct, incorrect, and premature). While there is not a systematic deviation as was seen with optogenetic inactivation of the superior colliculus (Cavanaugh et al., 2012), saccades show a broader spread of endpoints in the laser trials than in the trials without illumination.

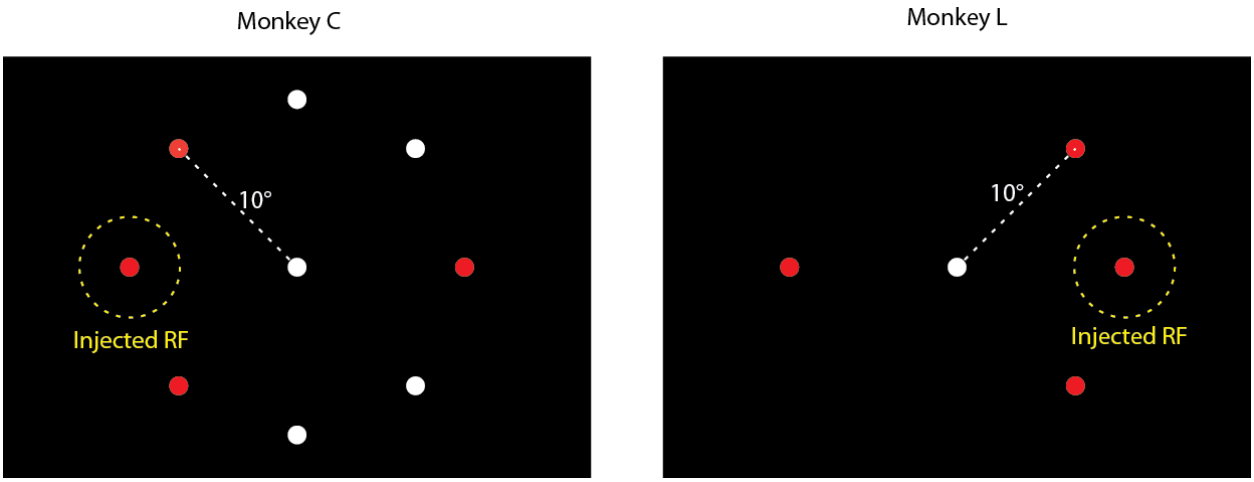

Supplementary Figure 16. Injection fields and target presentation locations for both monkeys
The receptive field corresponding to the center of the injection site is denoted by a dashed yellow circle. All possible target locations (10 degrees eccentric to center) are shown; however, only one target appeared per trial. The central fixation dot appeared on every trial. Both the target and the fixation dot were shown as white 1 degree diameter circles. In the diagram above, targets that were presented only with sham illumination are shown in white; those with both sham and laser illumination are shown in red. More targets were shown for monkey C than for monkey L due to differences in the animal's facility with the task. After the first day of inactivation, monkey L began to avoid targets on the injected side during testing (but not during calibration, implying a behavioral issue rather than physical damage). Consequently, only target locations in which we also illuminated were presented to monkey L subsequently. As shown above, this included the injected RF, the two adjacent target locations, and the target location 180 degrees opposite to the injected RF. Because the task was more difficult for monkey L at baseline, the error rates for targets on the side of the injected RF (which had 3 targets) were higher than those with for the contralateral side, which only had one target.

Supplementary Note

The light power density (mW /mm^2) on the surface of the ruby sphere as a function of fluence rate (photons / second) can be expressed as shown in Equation 1.

$$\Phi_{rs} = m*x / C \quad (1)$$

Where Φ_{rs} is light power density on the surface of the ruby sphere probe, x is fluence rate (photons / second) at the ruby wavelength(s), C is a constant correction factor determined to be 3.08 as shown below, and m is the probe- and wavelength-specific slope of the linear curve fit during the isometric probe calibration. Note that the y-intercept for that linear curve fit is set to 0.

The constant correction factor, C, is determined via Equation 2.

$$C = (1 + f_{H2O\text{-}cortex})* A_{cross\ section} / (A_{surface} *(1 - f_{blocked})) \quad (2)$$

Where $\boldsymbol{f_{H2O\text{-}cortex}}$ is the fraction by which calibration in water over estimates photon counts in cortex, $\mathbf{A_{cross\ section}}$ is the cross-sectional area of the ruby sphere (πr^2), the area over which collimated light is applied, $\mathbf{A_{surface}}$ is the surface area of the ruby sphere over which it (theoretically) can absorb photons ($4\pi r^2$), the area over which light is applied in vivo, and $\mathbf{f_{blocked}}$ is the fraction of the ruby sphere probe surface area that is blocked by the attached optical fiber and cannot absorb photons. $\mathbf{A_{cross\ section}}$, $\mathbf{A_{surface}}$, and $\mathbf{f_{blocked}}$ are all geometric properties of the isometric probe; however, the derivation of $\boldsymbol{f_{H2O\text{-}cortex}}$ is a bit more nuanced and, thus, explained below.

The difference in the refractive indices of water (n_{H2O} = 1.33) and the ruby (n_{ruby} = 1.77, provided by Edmund Optics) is slightly larger than the difference in the refractive indices of cortex (n_{cortex} = 1.37) (87) and the ruby. Thus, the critical angle in for the ruby in water is slightly smaller than the critical angle in cortex. The critical angle for total internal reflection of photons inside the ruby in both air and water was determined using **Equations 3** and **4.**

$$\Theta_{critical\_H2O} = arc(n_{H2O} / n_{ruby}) \quad (3)$$

$$\Theta_{critical\_cortex} = arc(n_{cortex} / n_{ruby}) \quad (4)$$

Snell's law was used to derive an expression for the angle of transmission, Θ_t, relative to the incident angle Θ_i (**Equations 5 and 6**).

$$\Theta_{t\_H2O} = \arcsin(n_{ruby} * \sin(\Theta_i) / n_{H2O}) \quad (5)$$

$$\Theta_{t\_cortex} = \arcsin(n_{ruby} * \sin(\Theta_i) / n_{cortex}) \quad (6)$$

Fresnel's Equations were rearranged to get reflection and transmission coefficients as a function of the incident angle for both the parallel and perpendicular cases as shown in **Equations 7 -10**. The terms parallel and perpendicular are relative to the plane of incidence.

$$\boldsymbol{R_{||}} = \frac{\boldsymbol{tan(\Theta i - \Theta t)}}{\boldsymbol{tan(\Theta i + \Theta t)}} \quad (7)$$

$$\boldsymbol{R_{\perp}} = \frac{\boldsymbol{sin(\Theta i - \Theta t)}}{\boldsymbol{sin(\Theta i + \Theta t)}} \quad (8)$$

$$\boldsymbol{T_{||}} = \frac{\boldsymbol{2*sin(\Theta t)*cos(\Theta i)}}{\boldsymbol{sin(\Theta i+\Theta t)*cos(\Theta i-\Theta t)}} \quad (9)$$

$$T_{\perp} = \frac{2*sin(\theta t)*cos(\theta i)}{sin(\theta i+\theta t)} \quad (10)$$

The percentages of light reflected and transmitted for a given incident angle were determined using the conservation of energy and then integrated over all possible incident angles to yield an overall percentage of photons emitted by the ruby sphere and then transmitted out of the ruby sphere back to the medium. In **Equation 11** below, the first term represents the fraction of fluoresced photons that are reflected back into the ruby sphere when emitted angles are less than the critical angle. The second term represents the angles over which 100% of photons remain in the ruby sphere.

$$\int_{\theta_i=0°}^{\theta_i=\theta_c} r(\theta_i)d\theta_i + \int_{\theta_i=\theta_c}^{\theta_i=90°} d\theta_i \quad (11)$$

These equations were solved empirically in MATLAB using $d\theta_i$ = 1°. It was determined empirically that water yields a photon count 3.8% higher than expected in cortex. This procedure was repeated for measurements and estimations in air v. water as well to confirm the correction. Theoretically, air should give a photon count 29.3% higher than expected in water and the measurements were 28.2 +/- 2.6% (standard error) higher in water than in air, which empirically confirms the validity of this theory-derived correction.

Supplementary Methods

Large-volume illuminator quality control. To ensure uniform light emission along the etched fiber tip, the illuminator was lowered with a micromanipulator (Siskiyou) into an integrating sphere (ThorLabs) in 500 µm increments through a diaphragm of custom shielding (light absorbing foil on the outside, aluminum foil facing inward) with a 26-gauge hole, sized such that no ambient light or light from parts of the fiber above the sphere could enter the integrating sphere. The total light power output was measured along the length of the illuminator and plotted as a function of how far the illuminator had been lowered into the integrating sphere. To confirm that the large-volume illuminator does not lose light energy due to its geometry, light power measurements from a flat cleaved optical fiber and the illuminator were compared under identical input conditions. After initial tests showed identical total light power output for the current illuminator and flat-cleaved fibers, this testing was not continued.

Isometric light probe construction. A 300 µm diameter spherical ruby ball lens (Edmund Optics) was centrally affixed to the flat-cleaved, polished end of a 400 µm diameter multimode optical fiber (ThorLabs, NA = 0.48) with optically-transparent, UV curable adhesive (NT37-322, Edmund Optics). An SMA connector was fixed to the other end of fiber (SMA904, ThorLabs). The isometric light probe (**Fig. S2**) was then coupled to a CCD spectrometer (Ocean Optics) via the SMA connection. After subtracting out a dark spectrum and correcting for non-linearity, light probe fluorescence was measured with the CCD spectrometer and recorded with SpectraSuite software (Ocean Optics) running on a PC. All recorded spectra were saved in their raw form without averaging. To prevent saturation near the ruby wavelength (690 - 695 nm), the spectrometer integration duration was adjusted in the range of 3 ms to

3 s, with most integration times in the 0.1 to 1 s range. Only the ruby peak was used in analysis. All photon counts were converted to fluence rates with units of photons/second offline.

Isometric probe calibration. The linear relationship between incident light power density at the test wavelength and induced ruby fluorescence was determined for each probe (**Fig. S4**). A beam of collimated light was generated by coupling a DPSS (532 nm and 635 nm, SLOC) or diode (473 nm, Vortran) laser to a large-diameter collimator (ThorLabs) via a 200µm diameter (NA = 0.22) multimode FC/PC terminated fiber (ThorLabs). The collimator was fixed in an externally threaded optic mount adapter (SM1P1, Thor Labs), and the external threading was screwed into a custom iris made of light-absorbing, black ABS plastic and coated with a light absorbing paint (Krylon). The custom iris was mounted and aligned to focus the beam centrally on a beam profiler (ThorLabs) that had been calibrated for absolute light power measurements. After collecting the total light power and beam uniformity measurements, a beam of collimated light, at light power densities of 0.5 to 4.5 mW / mm^2 in 0.25 mW / mm^2 increments, was applied to the light probe in water via a custom-built water bath. A linear relationship was determined between incident light power density and the emitted ruby photon count. The emitted ruby photon count was defined as the sum of all photons in the 0.47 nm-wide bin with peak amplitude between 693 nm and 697 nm. The slope was corrected to account for the slight difference in the refractive indexes of the brain (n = 1.37) and water (n = 1.33) and for the difference in the angle between the light source and probe during calibration (90°) and testing (72°). Each calibration was performed with exactly the same probe and light color as was used in testing. The probe was initially connected to the spectrometer for calibration and the connection was maintained until the end of testing with that probe.

Planar illuminator. A flat-cleaved and polished 1.5 mm diameter (NA = 0.5) plastic optical fiber (Industrial Fiber Optics) was affixed centrally in a custom, 3D printed aligner. For red (635 nm) and green (532 nm) light tests, an analog, fiber-coupled DPSS laser was connected to a TTL-controlled optical shutter (OzOptics) via a 200 µm diameter (NA = 0.22) multimode FC/PC terminated fiber. For 473 nm light, a fiber-coupled diode laser (Vortran) was used. The output from the shutter was FC coupled to the planar illuminator. The light power output from the planar illuminator was measured prior to each testing session by lowering it into an integrating sphere (ThorLabs) with attached power meter (ThorLabs) in 0.25 mm steps. The planar illuminator was used to approximate a wide collimated-beam source because using an actual wide collimated beam source was not physically possible in the *in vivo* preparation. In order to get a collimator with uniform light power output over a 1.5 mm diameter area, the collimator itself would need to be much larger than the mouse's head and only the very center of the collimated beam would be uniform enough for testing. While we initially attempted to use the iris with a very small aperture and large physical footprint that was used for calibration for the in vivo prep, we found it was not practical. Thus, we used a planar illuminator. Instead we profiled the beam of the planar illuminator and found it to be of uniform output (+/- 10%) over a centrally located 1 mm^2 area in the center of the beam even at a distance 8 mm away.

Monte Carlo Modeling. Monte Carlo modeling was performed in MATLAB using the Henyey-Greenstein anisotropic scattering model, 1e6 photons launched per voxel, and voxel size 50µm x 50µm x 50µm, as described previously.[28] Absorption and scattering coefficients of 2.14 cm^{-1} and 6.61 cm^{-1}, respectively, were used, as determined for 635 nm light. All illuminators had NA=0.5, as this is a property of the

optical fiber used (Industrial Fiber Optics, Inc.) NA =0.5 yields a half opening angle of 30 degrees. The novel illuminator was modeled as two 3mm long sheets of light angled as per the tip with a 30 degree downward bias, as per the NA. In a 3D model, these lines of light would be rotated in all direction, but in **Fig. S9** we only show the middle voxel, as its diameter (50 µm), corresponding to the diameter of a large neuron. Light exiting out the base of the new illuminator is ignored for simplicity and based on calibration data demonstrating that at least 90% of light, and typically more, exits out the sides, not the tip. The conventional optical fiber is shown at the middle voxel with equal light power density to the novel illuminator in **Fig. S9**. The planar illuminator was modeled at its diameter of 1.5mm with NA=0.5. In **Fig S7**, the middle 6 voxels of the planar illuminator model were summed to yield the light distribution over the 300 µm diameter of the isometric light probe.